The Astrophysical Journal, 812:153 (19pp), 2015 October 20 doi:10.1088/0004-637X/812/2/153

FRONTIER FIELDS CLUSTERS: CHANDRA AND JVLA VIEW OF THE PRE-MERGING CLUSTER MACS J0416.1-2403

G. A. Ogrean[1,18], R. J. van Weeren[1,19], C. Jones[1], T. E. Clarke[2], J. Sayers[3], T. Mroczkowski[2,20], P. E. J. Nulsen[1], W. Forman[1], S. S. Murray[1,4], M. Pandey-Pommier[5], S. Randall[1], E. Churazov[6,7], A. Bonafede[8], R. Kraft[1], L. David[1], F. Andrade-Santos[1], J. Merten[9], A. Zitrin[3,18], K. Umetsu[10], A. Goulding[1,11], E. Roediger[1,8,21], J. Bagchi[12], E. Bulbul[1], M. Donahue[13], H. Ebeling[14], M. Johnston-Hollitt[15], B. Mason[16], P. Rosati[17], and A. Vikhlinin[1]
[1] Harvard-Smithsonian Center for Astrophysics, 60 Garden Street, Cambridge, MA 02138, USA; gogrean@cfa.harvard.edu
[2] U.S. Naval Research Laboratory, 4555 Overlook Avenue SW, Washington, DC 20375, USA
[3] Cahill Center for Astronomy and Astrophysics, California Institute of Technology, MC 249-17, Pasadena, CA 91125, USA
[4] Department of Physics and Astronomy, Johns Hopkins University, 3400 N. Charles Street, Baltimore, MD 21218, USA
[5] Centre de Recherche Astrophysique de Lyon, Observatoire de Lyon, 9 av Charles André, F-69561 Saint Genis Laval Cedex, France
[6] Max Planck Institute for Astrophysics, Karl-Schwarzschild-Str. 1, D-85741, Garching, Germany
[7] Space Research Institute, Profsoyuznaya 84/32, Moscow, 117997, Russia
[8] Hamburger Sternwarte, Universität Hamburg, Gojenbergsweg 112 21029 Hamburg, Germany
[9] Department of Physics, University of Oxford, Keble Road, Oxford OX1 3RH, UK
[10] Institute of Astronomy and Astrophysics, Academia Sinica, P.O. Box 23-141, Taipei 10617, Taiwan
[11] Department of Astrophysical Sciences, Princeton University, Princeton, NJ 08544, USA
[12] Inter University Centre for Astronomy and Astrophysics, (IUCAA), Pune University Campus, Post Bag 4, Pune 411007, India
[13] Department of Physics and Astronomy, Michigan State University, East Lansing, MI 48824, USA
[14] Institute for Astronomy, University of Hawaii, 2680 Woodlawn Drive, Honolulu, HI 96822, USA
[15] School of Chemical & Physical Sciences, Victoria University of Wellington, P.O. Box 600, Wellington 6014, New Zealand
[16] National Radio Astronomy Observatory, 520 Edgemont Road, Charlottesville, VA 22903, USA
[17] Department of Physics and Earth Science, University of Ferrara, Via G. Saragat, I-1-44122 Ferrara, Italy
Received 2015 May 15; accepted 2015 August 31; published 2015 October 20

ABSTRACT

Merging galaxy clusters leave long-lasting signatures on the baryonic and non-baryonic cluster constituents, including shock fronts, cold fronts, X-ray substructure, radio halos, and offsets between the dark matter (DM) and the gas components. Using observations from *Chandra*, the Jansky Very Large Array, the Giant Metrewave Radio Telescope, and the *Hubble Space Telescope*, we present a multiwavelength analysis of the merging Frontier Fields cluster MACS J0416.1-2403 ($z = 0.396$), which consists of NE and SW subclusters whose cores are separated on the sky by ∼250 kpc. We find that the NE subcluster has a compact core and hosts an X-ray cavity, yet it is not a cool core. Approximately 450 kpc south–southwest of the SW subcluster, we detect a density discontinuity that corresponds to a compression factor of ∼1.5. The discontinuity was most likely caused by the interaction of the SW subcluster with a less massive structure detected in the lensing maps SW of the subcluster's center. For both the NE and the SW subclusters, the DM and the gas components are well-aligned, suggesting that MACS J0416.1-2403 is a pre-merging system. The cluster also hosts a radio halo, which is unusual for a pre-merging system. The halo has a 1.4 GHz power of $(1.3 \pm 0.3) \times 10^{24}$ W Hz^{-1}, which is somewhat lower than expected based on the X-ray luminosity of the cluster if the spectrum of the halo is not ultra-steep. We suggest that we are either witnessing the birth of a radio halo, or have discovered a rare ultra-steep spectrum halo.

Key words: galaxies: clusters: individual – galaxies: clusters: intracluster medium – X-rays: galaxies: clusters

1. INTRODUCTION

Galaxy clusters grow by merging with other clusters and by accreting smaller mass structures from the intergalactic medium. Signs of these interactions are imprinted in the intracluster medium (ICM) and detected in X-ray observations as cold fronts, shock fronts, turbulence, and substructure in the ICM (e.g., Markevitch & Vikhlinin 2007; Randall et al. 2008a; Zhuravleva et al. 2015). Other footprints of cluster interactions can be seen in the radio band as halos and relics (e.g., Feretti et al. 2012). If the merger is not in the plane of the sky, mergers can be detected in optical observations based on multiple peaks in the radial velocity distribution and in the spatial galaxy distribution. Furthermore, comparison of X-ray and optical/lensing data also reveals signatures of merging events, most notably as offsets between the dark matter (DM) and the gas components of the colliding clusters (e.g., Markevitch et al. 2004; Clowe et al. 2006; Randall et al. 2008b; Merten et al. 2011; Dawson et al. 2012).

Radio halos, which have been detected in some mergers, are diffuse synchrotron-emitting sources with low surface brightness, steep spectral indices ($\alpha < -1$, $S_\nu \propto \nu^\alpha$), and typical sizes of ∼1 Mpc. Because of their steep radio spectra, low-frequency radio observations play an important role in characterizing their properties. Two main models have been proposed to explain the origin of such halos:

1. *Reacceleration by turbulence*: Large-scale turbulence generated during the merger event supplies the energy required to reaccelerate fossil cosmic rays (CRs) back to relativistic energies, at which time they become synchrotron-bright (e.g., Brunetti et al. 2001; Petrosian 2001).

[18] Hubble Fellow.
[19] Einstein Fellow.
[20] National Research Council Fellow.
[21] Visiting Scientist.

2. *Acceleration by hadronic collisions*: Inelastic collisions between CR protons trapped in the gravitational potential of a cluster (e.g., originating from supernova explosions, active galactic nuclei (AGNs) outbursts, previous merger events, etc.) and thermal ICM protons give rise to a secondary population of CR electrons, which consequently are visible at radio frequencies (e.g., Blasi & Colafrancesco 1999; Dolag & Enßlin 2000).

However, hybrid models have also been postulated, in which radio halos may be produced by *turbulent reacceleration of secondary particles* resulting from hadronic proton–proton collisions (Brunetti & Blasi 2005; Brunetti & Lazarian 2011). The radio halos predicted by hybrid models are expected to be found in more relaxed clusters and to be underluminous for the masses of the hosting clusters (see also Brunetti & Jones 2014, for a review).

Hadronic radio halo models predict that magnetic fields should either be different in clusters with and without halos, or that gamma-ray emission should be detected in clusters hosting halos (e.g., Jeltema & Profumo 2011). However, there is no evidence that magnetic fields are stronger in clusters with radio halos (e.g., Bonafede 2010), and there has been no conclusive gamma-ray detection with the *Fermi* telescope (Ackermann et al. 2010). Therefore, current observational evidence disfavors hadronic models.

A textbook example of a merging cluster with a bright radio halo is the famous Bullet cluster, 1E 0657-56 (Elvis et al. 1992; Liang et al. 2000; Markevitch et al. 2002; Shimwell et al. 2014). *Chandra* has revealed that this system has a bullet-like subcluster core moving through the disturbed ICM of the main cluster (Markevitch et al. 2002). Immediately ahead of the core there is a density discontinuity associated with a cold front, while further out in the same direction there is a density discontinuity associated with a shock front (Markevitch et al. 2002; Owers et al. 2009). Recently, another shock front has been found on the opposite side of the Bullet cluster, behind the bullet-like core (Shimwell et al. 2015). *Chandra* observations of the Bullet cluster were followed up with optical/lensing data acquired, most notably, with the *Very Large Telescope* and the *Hubble Space Telescope* (*HST*). Chung et al. (2010) have shown that the redshift distribution of the Bullet cluster is bimodal, with two redshift peaks at $z \sim 0.21$ and $z \sim 0.35$, which imply a velocity difference $\sim$3000 km s^{-1} between the two merging subclusters. The gravitational lensing analysis has shown that the Bullet cluster is a dissociative merger, in which the essentially collisionless DM ($\sigma_{\rm DM} < 0.7$ g cm^{-2}, Randall et al. 2008b) has decoupled from the collisional ICM (Markevitch et al. 2004; Randall et al. 2008b). Lage & Farrar (2014) have combined the X-ray and lensing data with numerical simulations to constrain the merger scenario of the Bullet cluster.

Here, we present results from *Chandra*, Jansky Very Large Array (JVLA), and Giant Metrewave Radio Telescope (GMRT) observations of another merging galaxy cluster: the *HST* Frontier Fields[22] cluster MACS J0416.1-2403 ($z = 0.396$, Ebeling et al. 2001; Mann & Ebeling 2012). Optical and lensing studies of this cluster have been presented recently by, e.g., Zitrin et al. (2013, 2015), Schirmer et al. (2015), Jauzac et al. (2014), Grillo et al. (2015). Most recently, Jauzac et al. (2015) mapped the DM distribution of this merging system using strong- and weak-lensing data. Their analysis revealed two mass concentrations associated with the two main subclusters involved in the merger, plus two smaller X-ray-dark mass structures NE and SW of the cluster center. Jauzac et al. (2015) combined their lensing data with archival *Chandra* observations to study the offsets between the DM and the gas components. They report good DM-gas alignment for the NE subcluster, but a significant offset for the SW one. Based on the spectroscopic, lensing, and X-ray results, Jauzac et al. (2015) proposed two possible scenarios for the merger event in MACS J0416.1-2403—one pre-merging and one post-merging—but were unable to distinguish between the two.

The analysis presented herein combines significantly deeper *Chandra* observations with recently acquired JVLA and GMRT data and with the optical/lensing results reported by Jauzac et al. (2015) to improve our understanding of the merger event in MACS J0416.1-2403. The *Chandra* JVLA, and GMRT observations and data reduction procedures are described in Section 2. In Section 3 we discuss the background analysis of the *Chandra* data, and in Sections 4–7 we present the X-ray results. The radio results are presented in Section 8. In Section 9 we use the deeper *Chandra* data to revise the DM-gas offsets reported by Jauzac et al. (2015). In Section 10 we discuss the implications of our findings for the merger scenario of MACS J0416.1-2403. In Section 11 we examine the origin of the radio halo. A summary of our results is provided in Section 12.

Throughout the paper we assume a ΛCDM cosmology with $H_0 = 70\,{\rm km\,s^{-1}\,Mpc^{-1}}$, $\Omega_{\rm M} = 0.3$, and $\Omega_\Lambda = 0.7$. At the redshift of the cluster, $1'$ corresponds to approximately 320 kpc. Unless stated otherwise, the errors are quoted at the 90% confidence level.

2. OBSERVATIONS AND DATA REDUCTION

2.1. Chandra

The *HST* Frontier Fields cluster MACS J0416.1-2403 was observed with *Chandra* for 324 ks between 2009 June and 2014 December. A summary of the observations is given in Table 1.

The data were reduced using CIAO v4.7 with the calibration files in CALDB v4.6.5. The particle background level of the VFAINT observations was lowered by filtering out CR events associated with significant flux in the 16 border pixels of the 5×5 event islands. Soft proton flares were screened out from all observations using the *deflare* routine, which is based on the *lc_clean* code written by M. Markevitch. The flare screening was done using an off-cluster region at the edges of the field of view (FOV), which was selected to include only pixels located at distances greater than 2.5 Mpc from the cluster center and to exclude any point sources detectable by eye. The clean exposure times following this cleaning are listed in Table 1.

The inspection of an ObsID 10446 spectrum extracted from an off-cluster region showed a significant high-energy tail, which indicates that this observation is contaminated by flares that were not detected by the filtering routine. Given the relatively short exposure time of this observation, we decided to exclude ObsID 10446 from our analysis rather than attempt to model the flare component.

We reprojected the other five observations to a common reference frame, and created merged images in the energy bands 0.5–2, 0.5–3, 0.5–4, 0.5–7, and 2–7 keV. The exposure-

[22] http://www.stsci.edu/hst/campaigns/frontier-fields/

Table 1
Chandra Observations

ObsID	Observing Mode	CCDs On	Starting Date	Total Time (ks)	Clean Time (ks)
10446	VFAINT	0, 1, 2, 3, 6	2009 Jun 07	15.8	15.8
16236	VFAINT	0, 1, 2, 3, 6	2014 Aug 31	39.9	38.6
16237	FAINT	0, 1, 2, 3, 6	2013 Nov 20	36.6	36.3
16304	VFAINT	0, 1, 2, 3, 6	2014 Jun 10	97.8	95.2
17313	VFAINT	0, 1, 2, 3, 6	2014 Nov 28	62.8	59.9
16523	VFAINT	0, 1, 2, 3, 6	2014 Dec 19	71.1	69.1

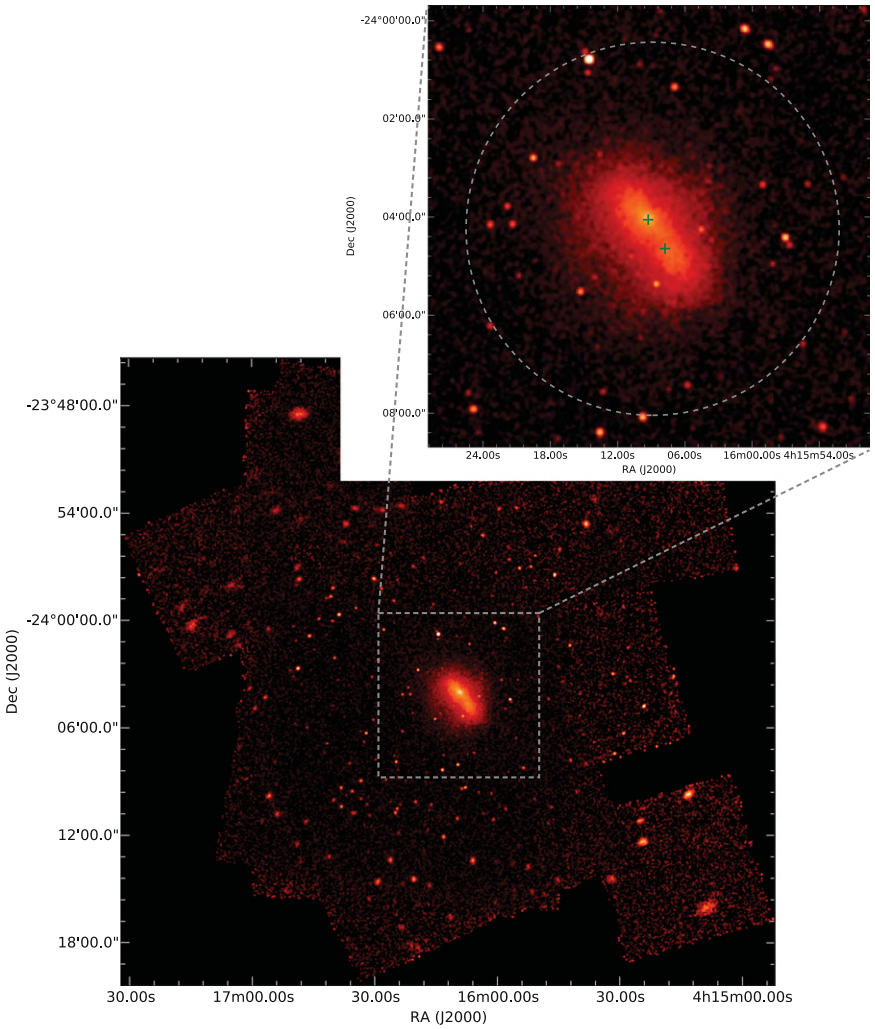

Figure 1. Logarithmic-scaled *Chandra* surface brightness map of the *HST* Frontier Fields Cluster MACS J0416.1-2403, in the energy band 0.5–4 keV. The image was binned by a factor of 4 (1 pixel ≈2″), exposure-corrected, vignetting-corrected, and smoothed with a 2D Gaussian kernel of width 1 pixel × 1 pixel. The large image shows the mosaic of all the ObsIDs summarized in Table 1, while the top image zooms in on the brightest X-ray regions of the cluster, in a region of size 2.9 × 2.9 Mpc^2. The dashed gray circle marks the boundary of the R_{500} region of the cluster. Green crosses mark the centers of the dark matter halos of the NE and SW merging clusters (M. Jauzac 2015, private communication).

corrected, vignetting-corrected 0.5–4 keV mosaic image is shown in Figure 1. To detect point sources, we also created merged exposure map-weighted point-spread function images (ECF = 90%) in each of the five energy bands. Point sources were detected in the individual bands with the CIAO task *wavdetect*, using the merged maps, wavelet scales of 1, 2, 4, 8, 16, and 32 pixels, a sigma threshold of 5×10^{-7}, and ellipses with 5σ axes. A few additional point sources that were missed by *wavdetect* were selected by eye and excluded from the data. All point sources detected by *wavdetect* were excluded from the data very conservatively, using the elliptical region that covered the largest area among the five elliptical regions identified for the different energy bands.

2.2. JVLA

JVLA observations of MACS J0416.1-2403 were obtained in the L-band in the BnA, CnB, and DnC array configurations. The observations were recorded with the default wide-band L-band setup, giving 16 spectral windows each having 64

Table 2
JVLA L-band Observations

	BnA-array	CnB-array	DnC-array
Observation dates	2014 Jan 25	2015 Jan 12	2014 Sep 19
Frequency coverage (GHz)	1–2	1–2	1–2
On source time (hr)	0.6	3.2	1.5
Correlations	full stokes	full stokes	full stokes
Channel width (MHz)	1	1	1
Visibility integration time (s)	2	3	5

channels, covering the entire 1–2 GHz band. An overview of the observations is given in Table 2.

The data were calibrated with the Common Astronomy Software Applications (CASA) package version 4.2.1 (McMullin et al. 2007). As a first step we flagged data affected by radio frequency interference (RFI) using AOFlagger (Offringa et al. 2010), after correcting for the bandpass shape. Data affected by other problems and antenna shadowing were flagged as well. After flagging, we applied the pre-determined elevation dependent gain tables and antenna offset positions. The data were Hanning smoothed.

We determined initial gain solutions using 10 channels at the center of the spectral windows for the primary calibrators 3C147 and 3C138. We then re-calibrated the bandpass and obtained delay terms (`gaintype = ''K''`) using the unpolarized calibrator 3C147. A next step consisted of calibration of the cross-band delays (`gaintype = ''KCROSS''`) using the polarized calibrator 3C138. We then solved again for the gains on the primary calibrators but now using all channels. The channel dependent leakage corrections were found using 3C147 and the polarization angles were set using 3C138. The gains were again re-determined for all calibrator sources which included the phase calibrator J0416-1851. Finally, the flux density-scale was bootstrapped from the primary calibrators to J0416-1851 and the calibration solutions were applied to the target field.

To refine the calibration for the target field, we performed three rounds of phase-only self-calibration and two final rounds of amplitude and phase self-calibration. W-projection (Cornwell et al. 2005, 2008) was employed during the imaging, taking the non-coplanar nature of the array into account. The self-calibration was independently performed for the three different data sets from the different array configurations. The full bandwidth was imaged using MS-MFS clean (`nterms = 2`; Rau & Cornwell 2011). Briggs (1995) weighting with a `robust` factor of −0.75 was used for self-calibration. Clean masks were used, which were made with the PyBDSM source detection package (Mohan & Rafferty 2015). The value of the chosen `robust` parameter was a compromise between sensitivity and approximately matching the GMRT resolution (see the next subsection).

After the self-calibration, the three data sets were combined. One final round of self-calibration was carried out on the combined data set. The final images were corrected for the primary beam attenuation.

In addition, we imaged the data set using an inner uv-range cut of 4.3 kλ (corresponding to a scale of about 1′, or 320 kpc) and `robust = 0` weighting. This model was then subtracted from the visibility data to allow a search for diffuse emission in the cluster. We imaged the data set with the emission from compact sources subtracted using a Gaussian uv-taper of 20″ and employing multi-scale clean (Cornwell 2008). An overview of the resulting image properties, such as root mean square (rms) noise and resolution are given in Table 3.

2.3. GMRT

GMRT 610 MHz data for MACS J0416.1-2403 were collected on 2013 December 3, using 26 antennas. The on-source time was 5.0 hr, and a total bandwidth of 33.3 MHz (RR correlations only), split into 512 channels, was recorded. NRAO's Astronomical Image Processing System (AIPS) was used to carry out the initial calibration of the visibility data set. The primary calibrator 3C 147 was used to set the flux density scale and derive the bandpass solutions for all the antennas. The source J0409-179 was observed for 6-minutes scans at intervals of ∼25 minutes and used as the secondary phase and gain calibrator. About 20% of the data, mostly from short baselines, were affected by RFI and subsequently flagged. Gain solutions were obtained for the calibrator sources and together with the bandpass solutions applied to the target field. In total, 480 of the 512 channels were used; the rest of the channels were discarded as they were too noisy due to the bandpass roll-off. The 480 channels were averaged down to 48 channels to reduce the size of the data.

The visibility data were then imported into CASA to refine the calibration via the process of self-calibration. Three rounds of phase-only self-calibration and two final rounds of amplitude and phase self-calibration were applied. The phase-only self-calibration was carried out on a 30 s timescale. The amplitude and phase self-calibration was carried out on a 2 minute timescale, pre-applying the phase-only solutions before solving for the amplitude and phases on the longer 2 minute timescale. We employed W-projection during the imaging and used `nterms = 2`.

A map with Briggs (`robust = 0.5`) weighting of the field was produced, which resulted in a resolution of $7\farcs6 \times 4\farcs0$ and an rms noise level of 54 μJy beam^{-1} (Table 3). Similarly to the JVLA L-band data reduction, we imaged the data set using an inner uv-range cut of 4.3 kλ to obtain a model of the compact sources in the field. After subtracing this model from the uv-data, we re-imaged with uniform weighting and a Gaussian uv-taper to obtain a beam size of 20″.

2.4. VLITE

A new commensal observing system called the VLA Low Band Ionospheric and Transient Experiment (VLITE)[23] has been developed for the NRAO JVLA (Clarke et al. 2015, in preparation) and was operational during the observations of MACS J0416.1-2403. The VLITE correlator is a custom designed DiFX software correlator (Deller et al. 2011). The system processes 64 MHz of bandwidth centered on 352 MHz with two second temporal resolution and 100 kHz spectral resolution. VLITE operates during nearly all pointed JVLA observations with primary science goals at frequencies above 1 GHz, providing data simultaneously for 10 JVLA antennas using the low band receiver system (Clarke et al. 2011).

[23] http://vlite.nrao.edu/

Table 3
Radio Imaging Parameters

Instrument	Weighting	Resolution (arcsec × arcsec)	rms Noise (μJy beam^{-1})
JVLA 1.5 GHz	Briggs −0.75	7.8 × 5.5	14
JVLA 1.5 GHz	uniform +20″ Gaussian taper	18 × 18	20
GMRT 610 MHz	Briggs 0.5	7.6 × 4.0	54
GMRT 610 MHz	uniform +20″ Gaussian taper	20 × 20	360
VLITE 340 MHz	Briggs 0.0	45.7 × 31.1	2000

We processed the CnB configuration VLITE observation of MACS J0416.1-2403 from 2015 January 12 using a combination of the Obit software package (Cotton 2008) and AIPS (van Moorsel et al. 1996). VLITE data at frequencies $\nu > 360$ MHz were removed due to the presence of strong RFI from a satellite downlink that is present during most operations. The data at $\nu < 360$ MHz were flagged using the AIPS program RFLAG to remove the majority of the remaining RFI. The bandpass was flattened using observations of several calibrators taken near the time of the observations (3C48, 3C138, 3C147, and 3C286). These calibrator sources were taken in the same primary observing band as MACS J0416.1-2403. The delays were determined using these same calibrators. The delay corrected data then were flux calibrated using these same calibrator sources. No phase calibrator is required for low band observations due to the large FOV (FWHM ∼2.°3 at 320 MHz) and typical presence of sufficiently strong sources in the field that allow for self-calibration.

The initial imaging of the target field revealed additional RFI that was identified in the residual data set after all compact sources had been subtracted from the uv data. These baselines were excised from the full data set and we further refined the calibration through four rounds of phase-only self-calibration. Non-coplanar effects were taken into account in the imaging steps using small facets to make a fly-eye image of the full field out to the FWHM with additional facets placed on bright sources out to 20° from the field center. Data were imaged using small clean masks placed around all sources. The final VLITE image of MACS J0416.1-2403 has a resolution of 45.″7 × 31.″1 and an rms noise of 2.0 mJy beam^{-1}. The image was made using a Briggs robust parameter of 0 (see Table 3).

3. X-RAY FOREGROUND AND BACKGROUND MODELING

We analyzed the *Chandra* data using the Group F stowed background event files, which are appropriate for observations taken after 2009 September 21. The particle background was subtracted from the data, while the foreground and background sky components were modeled from off-cluster regions. For each of the cluster ObsIDs, we created corresponding stowed background event files, applied the VFAINT cleaning to those associated with cluster observations taken in this observing mode, and renormalized the stowed background observations such that the count rates in the energy band 10–12 keV matched those of the corresponding observation in the same energy band. We modeled the sky components as the sum of unabsorbed thermal emission from the Local Hot Bubble (LHB; APEC component with $T \approx 0.1$ keV; Snowden 1998), absorbed thermal emission from the Galactic Halo (GH; APEC component with $T \approx 0.2$ keV; Henley et al. 2010), and absorbed non-thermal emission from undetected point sources in the FOV (power-law component with index 1.41 ± 0.06; De Luca & Molendi 2004). The redshifts of the foreground components were set to 0, while the abundances were set to solar values assuming the abundance table of Anders & Grevesse (1989). The hydrogen column density was fixed to 2.89×10^{20} atoms cm^{-2} (Kalberla et al. 2005). The *Chandra* spectra were fit in the energy band 0.5–7 keV using XSPEC v12.8.2—the lower limit was chosen to avoid calibration uncertainties at low energies, and the upper limit to increase the signal-to-noise ratio (S/N).

When fitting the *Chandra* spectra in the energy band 0.5–7 keV, the ∼0.1 keV LHB component cannot be constrained. Instead, we constrain this component using a *ROentgen SATellite* (*ROSAT*) All-Sky Survey (RASS) spectrum[24] corresponding to an annulus with radii 0.°15 and 1.°0 around the cluster. The *ROSAT* spectrum was fit in the energy band 0.1–2.4 keV, with the normalization of the power-law background component fixed to 8.85×10^{-7} photons keV^{-1} cm^{-2} s^{-1} arcmin^{-2} (Moretti et al. 2003). The temperatures and normalizations of the LHB and GH components were free in the fit. The results of the fit to the *ROSAT* spectrum are presented in Table 4.

Based on the *ROSAT* results, the parameters of the LHB components were fixed for the *Chandra* spectra. The five *Chandra* spectra were then fitted in parallel, assuming that they are described by the same foreground model. The power-law normalizations, on the other hand, were left to vary independently, in order to account for the varying exposure time across the merged observation that was used for point source detection. The energy sub-band 0.5–0.8 keV was ignored for ObsID 16237 due to negative spectral residuals caused by a change in the spectral shape of the background component that is not filtered by the VFAINT cleaning, which occurred between 2009 (the date of the Group F background files) and 2013 (the date of the observation; A. Vikhlinin 2015, private communication). The subtraction of the instrumental background resulted in small line residuals near the spectral positions of the Al Kα ($E \approx 1.49$ keV), Si Kα ($E \approx 1.75$ keV), and Au Mα, β ($E \approx 2.1$ keV) fluorescent instrumental lines. Therefore, we excluded from the spectra very narrow bands ($\Delta E = 0.10$ keV) surrounding these lines.

The best-fitting foreground and background parameters are summarized in Table 4. The spectra were grouped to have at least 1 count per bin, and the fit was done using the extended C-statistic[25] (Cash 1979; Wachter et al. 1979).

[24] https://heasarc.gsfc.nasa.gov/cgi-bin/Tools/xraybg/xraybg.pl
[25] https://heasarc.gsfc.nasa.gov/xanadu/xspec/manual/XSappendixStatistics.html

Table 4
Foreground and Background Spectral Models

Component	*Chandra*		*ROSAT*	
	T^{a}	$\mathcal{N}^{b}$	T^{a}	$\mathcal{N}^{b}$
LHB	0.10 ± 0.01^{c}	$9.32^{+0.62}_{-0.83} \times 10^{-7}$[c]	0.10 ± 0.01	$9.32^{+0.62}_{-0.83} \times 10^{-7}$
GH	$0.25^{+0.23}_{-0.08}$	$2.35^{+4.20}_{-1.66} \times 10^{-7}$	$0.22^{+0.05}_{-0.04}$	$6.74^{+3.44}_{-2.06} \times 10^{-7}$
Power-law ObsID 16236	...	$4.20^{+0.86}_{-0.73} \times 10^{-7}$	...	...
Power-law ObsID 16237	...	$2.17^{+0.76}_{-0.86} \times 10^{-7}$	...	...
Power-law ObsID 16304	...	$2.45^{+0.60}_{-0.59} \times 10^{-7}$	...	...
Power-law ObsID 17313	...	$3.70^{+0.86}_{-0.84} \times 10^{-7}$	...	...
Power-law ObsID 16523	...	$4.33^{+0.71}_{-0.69} \times 10^{-7}$	...	...

Notes.
[a] Temperature, in units of keV.
[b] Normalization, in units of cm^{-5} arcmin^{-2} for the thermal components, and in units of photons keV^{-1} cm^{-2} s^{-1} arcmin^{-2} for the non-thermal components.
[c] Fixed parameter.

4. GLOBAL X-RAY PROPERTIES

MACS J0416.1-2403 has been previously identified as a merging galaxy cluster at $z = 0.396$ (Mann & Ebeling 2012). The brightness of the NE subcluster core is significantly more peaked than that of the SW subcluster, which instead has a rather flat brightness distribution (Figure 1).

We determined the average cluster temperature by extracting spectra from a circular region of radius 1.2 Mpc (approximately R_{500}, Sayers et al. 2013) centered at $\alpha = 4^{h}\,16^{m}\,08\overset{s}{.}8$ and $\delta = -24^{\circ}\,04'\,14\overset{''}{.}0$ (J2000). The spectra extracted from the five *Chandra* ObsIDs were fit in parallel, assuming the cluster emission is described by a single-temperature thermal component.[26] For this global fit, the sky background parameters were fixed to the values listed in Table 4, and the redshift was fixed to 0.396. We found $T = 10.06^{+0.50}_{-0.49}$ keV and $L_{X,\,0.1-2.4\,keV} = (7.43 \pm 0.08) \times 10^{44}$ erg s^{-1}. The average cluster parameters are shown in Table 5.

Table 5
Cluster Properties in R_{500}

T (keV)	$10.06^{+0.50}_{-0.49}$
Z ($Z_{\odot}$)	$0.24^{+0.05}_{-0.04}$
$L_{X,0.1-2.4\,keV}$ (erg s^{-1})	$(7.43 \pm 0.08) \times 10^{44}$

5. MAPPING THE CLUSTER'S X-RAY PROPERTIES

5.1. Mapping of the ICM Temperature

We mapped the cluster properties using CONTBIN (Sanders 2006).[27] The merged *Chandra* image was adaptively binned in regions of ~3600 source plus sky background counts in the energy band 0.5–7 keV. The bins follow the surface brightness contours of the cluster, thus minimizing possible gas mixing in bins located near density discontinuities. Instrumental background and total spectra were extracted from regions corresponding to each bin, and grouped to have at least one count per bin. The net spectra were modeled as the sum of sky background components plus a single temperature absorbed thermal model (*phabs*×*APEC*) with free temperature and normalization. The metallicity was fixed to $Z = 0.24\,Z_{\odot}$ (see Section 4). The sky background emission was fixed to the model summarized in Table 4. The spectra extracted from the five *Chandra* data sets were fitted in parallel, with the temperatures and normalizations linked between the different ObsIDs. The fits were done using the extended C-statistic. The resulting temperature map is shown in Figure 2.

The temperature is high throughout the cluster, which causes the uncertainties on the measurements to be high. The temperature map does not show significant structure. Within the uncertainties, the temperatures out to ~400 kpc from the cluster center are consistent with ~10 keV.

5.2. Mapping of the ICM Pressure and Entropy

The electron number density can be derived either from the model normalization of the fitted spectrum, or from the surface brightness in the regions of interest. Extracting the number density from either of these quantities requires assumptions about the cluster geometry. Here, we estimated the electron number density from the surface brightness; we note that our results are unchanged when deriving the density from the spectral normalization.

The surface brightness, ζ, is essentially proportional to the emission measure,

$$\zeta \propto \int n_{e}^{2}\, dl \qquad (1)$$

where the integration is done along the line of sight and n_e is the electron number density. More accurately, the surface brightness is also temperature-dependent. This dependence introduces an uncertainty of $\lesssim$10% in the pressure and entropy maps, which is less than the uncertainties on the temperatures and does not affect our results.

[26] We tried adding an additional thermal component to fit the cluster emission, but the parameters of the second component could not be constrained.
[27] We also created temperature maps using the codes described by Churazov et al. (2003) and Randall et al. (2008a), and obtained consistent results at the 90% confidence level.

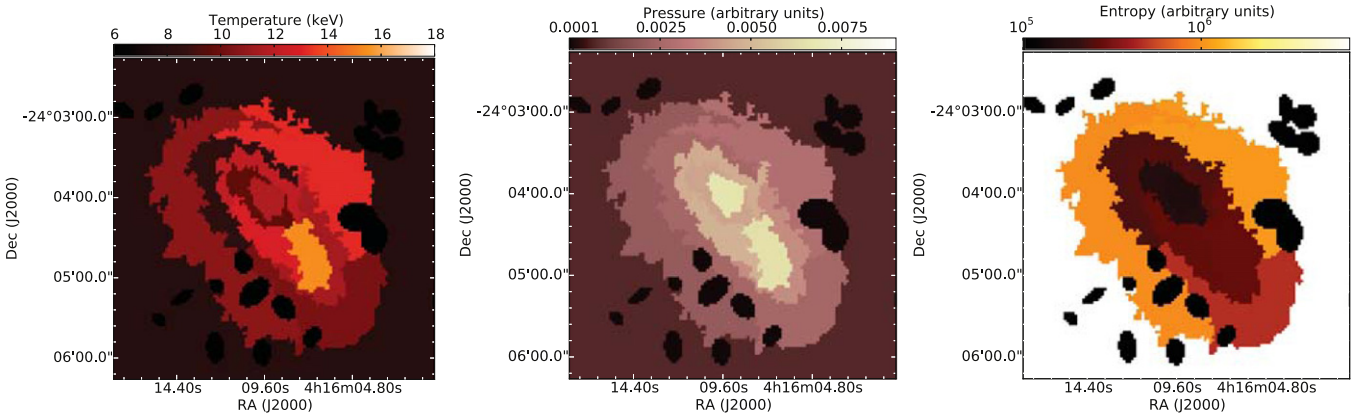

Figure 2. Temperature, pseudo-pressure, and pseudo-entropy maps of MACS J0416.1-2403. In all maps, black elliptical regions mark the regions from which point sources have been removed.

We approximated the density as $\zeta^{1/2}$, and defined the pseudo-pressure and pseudo-entropy as:

$$P = T\,\zeta_{0.5-2\ \mathrm{keV}}^{1/2}, \tag{2}$$

$$K = T\,\zeta_{0.5-2\ \mathrm{keV}}^{-1/3}. \tag{3}$$

The pseudo-pressure and pseudo-entropy maps are included in Figure 2.

Strong jumps in pressure and entropy would indicate the presence of strong density discontinuities in the ICM. However, neither the pressure map, nor the entropy map of MACS J0416.1-2403 shows evidence of such strong jumps between the regions. We note that while a pressure and entropy discontinuity can be seen between regions #3 and #0, the size of region #0 is too large for this result to truly indicate that there is a density discontinuity at the boundary of the two regions.

In Table 6 we list the best-fitting temperatures, spectral normalizations, and 0.5–2 keV count rates for the regions in Figure 2. The bin numbers necessary to relate Table 6 and Figure 2 are shown in Figure 3. An interactive version of the temperature map, which combines Figures 2, 3 and Table 6 is available at http://hea-www.cfa.harvard.edu/~gogrean/interactive/MACSJ0416_Tmap.html.

Table 6
Best-fitting Temperatures, Normalizations, and 0.5–2 keV Count Rates for the Regions in Figure 3

Bin Number	T^{a}	$\mathcal{N}^{b}$	$S_X{}^{c}$
0	$7.95^{+1.32}_{-0.92}$	$(2.24 \pm 0.06) \times 10^{-5}$	$(7.39 \pm 0.07) \times 10^{-6}$
1	$10.74^{+2.10}_{-1.37}$	$(1.70 \pm 0.05) \times 10^{-4}$	$(3.38 \pm 0.06) \times 10^{-5}$
2	$13.25^{+3.07}_{-2.32}$	$(2.31 \pm 0.07) \times 10^{-4}$	$(4.34 \pm 0.08) \times 10^{-5}$
3	$10.32^{+1.91}_{-1.35}$	$(2.77 \pm 0.08) \times 10^{-4}$	$(5.30 \pm 0.09) \times 10^{-5}$
4	$11.69^{+2.10}_{-1.46}$	$(1.63 \pm 0.05) \times 10^{-3}$	$(2.96 \pm 0.06) \times 10^{-4}$
5	$9.73^{+1.52}_{-1.24}$	$(9.80 \pm 0.29) \times 10^{-4}$	$(1.84 \pm 0.04) \times 10^{-4}$
6	$15.39^{+3.42}_{-2.87}$	$(9.03 \pm 0.23) \times 10^{-4}$	$(1.62 \pm 0.03) \times 10^{-4}$
7	$12.90^{+3.64}_{-2.15}$	$(7.13 \pm 0.22) \times 10^{-4}$	$(1.27 \pm 0.03) \times 10^{-4}$
8	$12.18^{+2.41}_{-1.90}$	$7.10^{+0.22}_{-0.21} \times 10^{-4}$	$(1.31 \pm 0.03) \times 10^{-4}$
9	$11.43^{+2.29}_{-1.65}$	$(5.51 \pm 0.17) \times 10^{-4}$	$(1.02 \pm 0.02) \times 10^{-4}$
10	$8.41^{+1.37}_{-0.90}$	$(4.12 \pm 0.13) \times 10^{-4}$	$(8.02 \pm 0.15) \times 10^{-5}$

Notes.
[a] Temperature, in units of keV.
[b] Spectral normalization, in units of $\mathrm{cm}^{-5}\,\mathrm{arcmin}^{-2}$.
[c] 0.5–2 keV count rate, in units of photons $\mathrm{cm}^{-2}\,\mathrm{s}^{-1}\,\mathrm{arcmin}^{-2}$.

6. PROPERTIES OF THE INDIVIDUAL SUBCLUSTERS

The merging history of the individual subclusters is closely related to their degree of disturbance. In the following two sections, we perform the imaging analysis of the NE and SW subclusters in order to characterize their merging states. For both subclusters, we created surface brightness profiles in sectors centered on the respective X-ray peaks, and attempted to model the profiles with isothermal β-models (Cavaliere & Fusco-Femiano 1976, 1978):

$$S(r) = S_0\left[1 + \left(\frac{r}{r_c}\right)^2\right]^{-3\beta+0.5} \tag{4}$$

where S_0 is the central surface brightness, r_c is the core radius, β is the beta parameter, and r is the radius from the cluster center.

Simple β-models provide good descriptions of the X-ray profiles of galaxy clusters that do not have strong ICM temperature gradients (e.g., Ettori 2000a, 2000b). Based on Figure 2, there are indeed no strong temperature gradients in the NE and the SW subclusters of MACS J0416.1-2403.

Before fitting, all the profiles were binned to a minimum of 1 count/bin. The fits used Cash statistics. Fitting was done using a modified version of the PROFFIT package[28] (Eckert et al. 2011). All the surface brightness profiles presented in the following subsections are in the energy band 0.5–4 keV. The profiles were instrumental background-subtracted, and exposure- and vignetting-corrected.

6.1. NE Subcluster

The sector used to create the surface brightness profile of the NE subcluster and the fits to this profile are shown in Figure 4. The sky background surface brightness level was determined by fitting a constant to the outer bins (radii 5′.0–10′.7) of the profile. The sky background level was kept fixed in the following fits. The very central part of the profile is significantly underestimated by the best-fitting β-model.

[28] Available upon request.

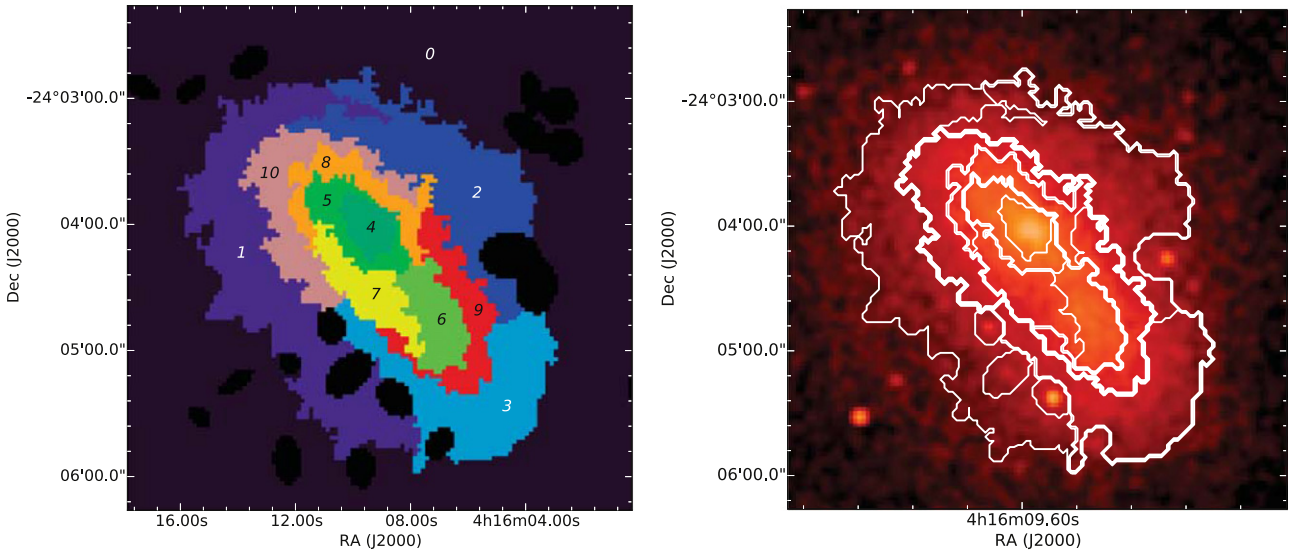

Figure 3. *Left:* The map shows the association of regions in Figure 2 with the fit values in Table 6. Numbers are region numbers. Black ellipses mark the regions where point sources have been removed. *Right:* Same surface brightness map as in Figure 1, with overlaid regions used for mapping the physical properties of the ICM.

Instead, the profile is described better by a double β-model:

$$S(r) = \sum_{i=1,2} S_{0,i}\left[1 + \left(\frac{r}{r_{c,i}}\right)^2\right]^{-3\beta+0.5}. \quad (5)$$

Double β-models provide good representations of cooling-core clusters (e.g., Jones & Forman 1984; Ota et al. 2013). However, the core of the NE subcluster in MACS J0416.1-2403 is far from cool, having a temperature >10 keV based on the temperature map in Figure 2. To constrain a possible cooler component, we examined the possibility that the projected temperature of the gas in bin #4 (see Figure 3) is increased due to the projection of hot gas onto the subcluster core. We modeled the spectrum of bin #4 with a two-temperature APEC model: one describing possible cool gas in the cluster center, and another describing hotter gas ($T > 10$ keV) in the cluster outskirts. The normalizations of the two components were free in the fit. The count statistics do not allow us to leave both temperatures free in the fit. Therefore, we left the temperature of the hot plasma free, and fixed the temperature of the core to 5 keV.[29] In the best-fitting model, the normalization of the cool component is about 5 times lower than that of the hot component, which implies that the gas density in the core is lower than the density right outside the core radius; such a density model is not physical. The two-temperature APEC model also provides no improvement in the statistics of the fit. If the core has a temperature <5 keV, then the normalization of the cool component would be even lower relative to the normalization of the hot component, so the core density would be even lower.

Cooler gas in the NE core could be masked by inverse Compton (IC) emission from the AGN hosted by the NE subcluster brightest cluster galaxy (BCG). To examine this possibility, we measured the temperature in an annulus with radii 32 and 64 kpc around the AGN in the NE BCG. The best-fitting temperature in this annulus is very high, $15.65^{+5.03}_{-3.22}$ keV. In a smaller circle with a radius of 35 kpc around the NE core, the best-fitting temperature is $10.54^{+3.00}_{-2.11}$ keV, and consistent with the temperature calculated in an annulus around the core. Therefore, we find no evidence that the NE core is cool.

From the best-fitting double β-model, we calculated the central density of the NE core to be $(1.4 \pm 0.3) \times 10^{-2}$ cm^{-3}. The density and temperature of the NE core hence imply a cooling time of $3.5^{+1.0}_{-0.9}$ Gyr, which further supports our conclusion that the NE subcluster cannot be classified as a cool core cluster based on currently available X-ray data.

To investigate if the double β-model shape of the NE profile is caused by substructure in a particular direction, we divided the NE sector shown in Figure 4 into three subsectors, and modeled the profile of each subsector with β- and double β-models. The fits are shown in Figure 5. For each of the subsectors, a double β-model describes the profile better than a single β-model at a confidence level >99.99%.

6.2. SW Subcluster

The surface brightness profile of the SW subcluster and the sector used in the extraction of this profile are shown in Figure 6. As for the NE profiles, the sky background profile was modeled by fitting a constant to the outer bins of the profile, in the range $r = 4\farcm5$–$10\farcm7$. Unlike the NE profiles, the SW profile is modeled well by a simple β-model. The fit is shown in Figure 6.

A weak edge in the profile can be seen at $r \sim 1\farcm5$. We divided the profile into three subsectors with equal opening angles (60°) to check whether the edge is seen along all three directions, and found that it is present only in the central subsector (position angles 280°–340°, measured from the W in a counterclockwise direction). To describe it, we fitted a projected broken power-law elliptical density model to the surface brightness profile between $r = 0\farcm5$–$4\farcm0$. The density

[29] A larger temperature would be unusual for a cool core.

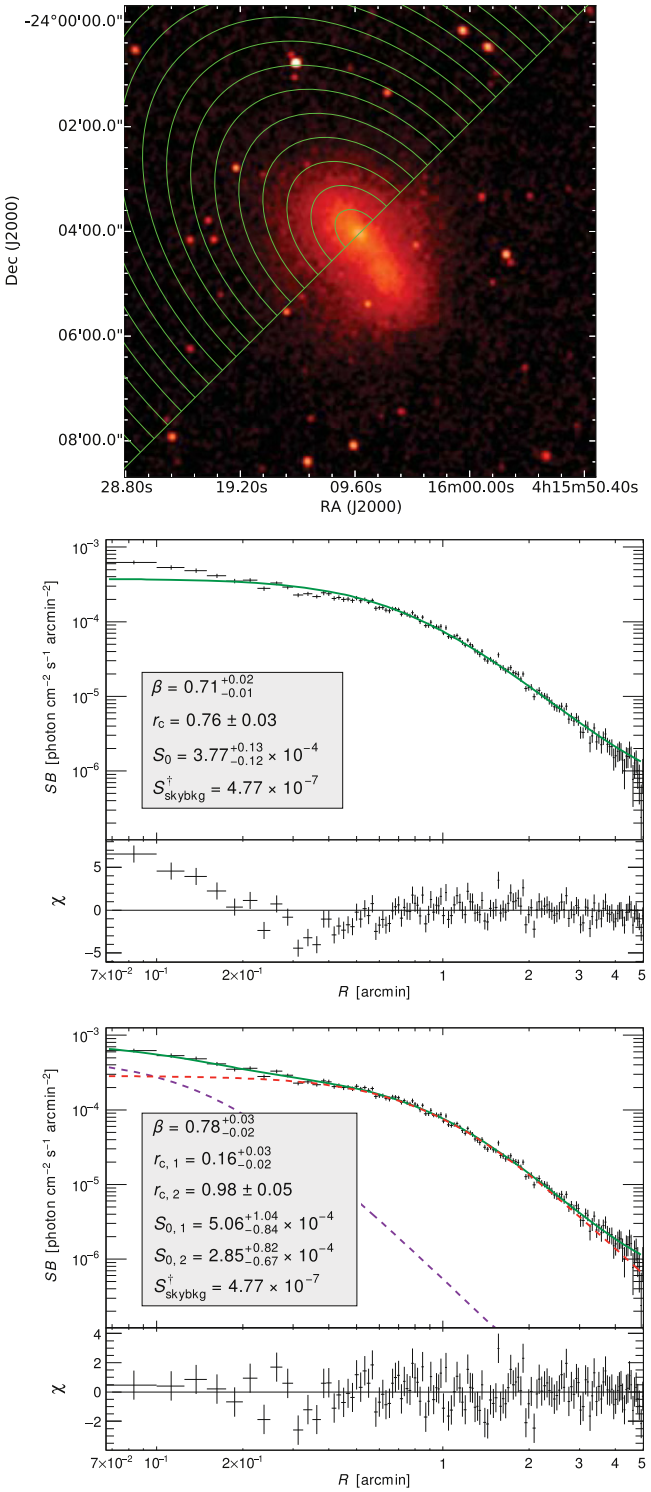

Figure 4. *Top:* Sector used to model the surface brightness of the NE subcluster. Annuli are drawn only to guide the eye and do not reflect the actual bin size used for the surface brightness profiles. *Middle:* β-model fit to the surface brightness profile of the NE subcluster. For clarity, the profile shown in this plot was binned to a uniform signal-to-noise ratio of 5. *Bottom:* Double β-model fit to the surface brightness profile of the NE subcluster. The individual β-models are shown with dashed lines. For clarity, the profile shown in this plot was binned to a have 200 counts per bin. The best-fitting model parameters are listed in the middle and bottom plots; radii units are arcmin, and surface brightness units are photon cm^{-2} s^{-1} arcmin^{-2}. Fixed parameters are shown with a superscripted †. The bottom panel shows the residuals of the fit.

model is defined as:

$$n(r) = \begin{cases} C\, n_0 \left(\frac{r}{r_d}\right)^{-\alpha}, & \text{if } r \leqslant r_d \\ n_0 \left(\frac{r}{r_d}\right)^{-\beta}, & \text{if } r > r_d \end{cases}, \quad (6)$$

where n is the electron number density, n_0 is the density immediately ahead of the density jump, C is the density compression, r is the distance from the center of the sector, r_d is the radius at which the density jump is located, and α and β are the indices of the two power-laws. The fit is shown in Figure 7. If the density discontinuity is a shock front, then its magnitude corresponds to a shock with Mach number $\mathcal{M} = 1.40^{+0.14}_{-0.12}$. Unfortunately, the count statistics are too poor to allow us to distinguish between a cold front and a shock front based on the temperature jump, and thus we cannot determine the nature of the surface brightness edge.

7. SUBSTRUCTURE IN THE ICM

The search for substructure in the ICM is motivated by the identification in the lensing maps of two less massive structures in addition to the main NE and SW subclusters (Jauzac et al. 2015). The positions of these mass structures are shown in Figure 8 and denoted by S1 and S2 for consistency with the notation of Jauzac et al. (2015). In the analysis of Jauzac et al. (2015), S1 and S2 were found to be X-ray-dark; however, the X-ray data presented here are ∼6 times deeper, which would make it easier to observe ICM substructure.

We searched for substructure using the unsharp-masked image of the cluster, which was created by dividing the difference of two 0.5–4 keV fluxed images convolved with Gaussians of widths 4″ and 10″ by their sum. The resulting image, shown in Figure 8, highlights substructure on scales of ∼20–50 kpc.[30] There is no excess X-ray emission at the positions of S1 and S2. However, the emission is elongated in the direction of both mass structures. In the south, the ICM appears elongated in the direction of S1, while in the north the emission is elongated along the line connecting the NE and SW subclusters and then appears to curve in the direction of S2. We note that if S1 and S2 have already merged with the NE and SW subclusters, the DM would have decoupled from the gas, and therefore we do not necessarily expect a spatial overlap between the DM and gas components.

Interestingly, the unsharp-masked image enchances a small cavity with a diameter ∼50 kpc NW of the core of the NE subcluster. We examined the significance of the cavity from the azimuthal surface brightness profile in an annulus around the cluster center. The annulus was divided in 14 partial annuli with equal opening angles. The partial annuli and the azimuthal surface brightness profile are shown in Figure 9. The azimuthal surface brightness profile is lowest in four partial annuli located NW of the NE core. The largest dip is in the partial annulus that crosses the middle of the X-ray cavity seen in the unsharp-masked image; the opening angles of this

[30] Smoothing with Gaussians of larger widths does not reveal additional substructure.

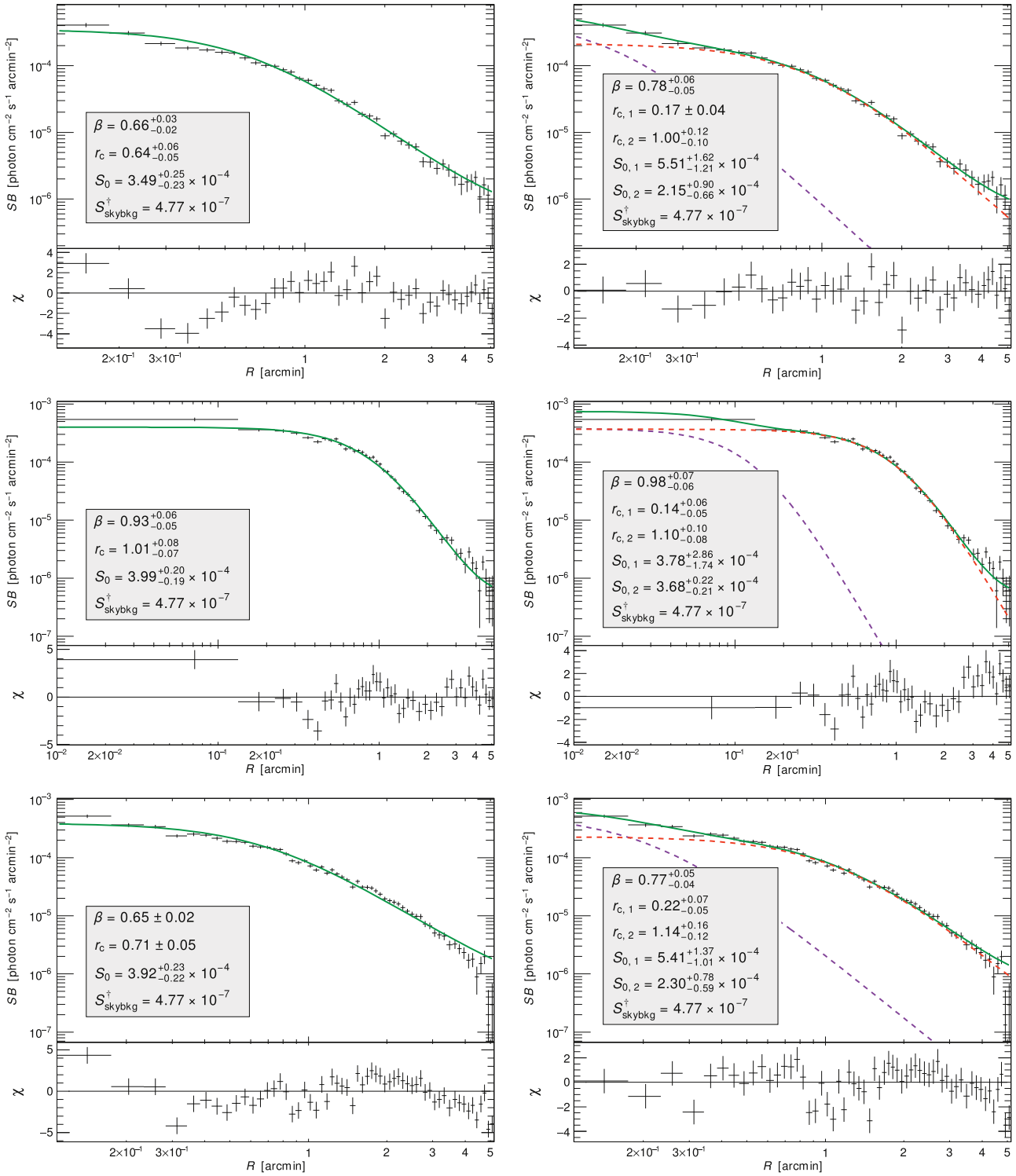

Figure 5. β-model (left) and double β-model (right) fits to the surface brightness profiles of the NE sectors with position angles of 45°–115° (top), 115°–155° (middle), and 155°–225° (bottom). The position angles are measured from W, in a counterclockwise direction. For all the profiles, a double β-model constitutes a better fit than a single β-model, with confidence levels of 4.4σ for the top profile, 3.3σ for the middle profile, and 6.4σ for the bottom profile. The individual β-models are shown with dashed lines. For clarity, all profiles shown have been regrouped in the plots to have 200 counts per bin. The best-fitting model parameters are listed on the plots; radii units are arcmin, and surface brightness units are photon cm^{-2} s^{-1} arcmin^{-2}. Fixed parameters are shown with a superscripted †. The bottom panel shows the residuals of the fit.

partial annulus are 51°–77°. No radio emission fills the X-ray cavity, but the cavity was likely inflated by the AGN hosted by the NE BCG (see Section 8).

8. RADIO RESULTS

The JVLA 1–2 GHz images reveal several compact sources in the cluster region (Figure 10). Two of these sources are

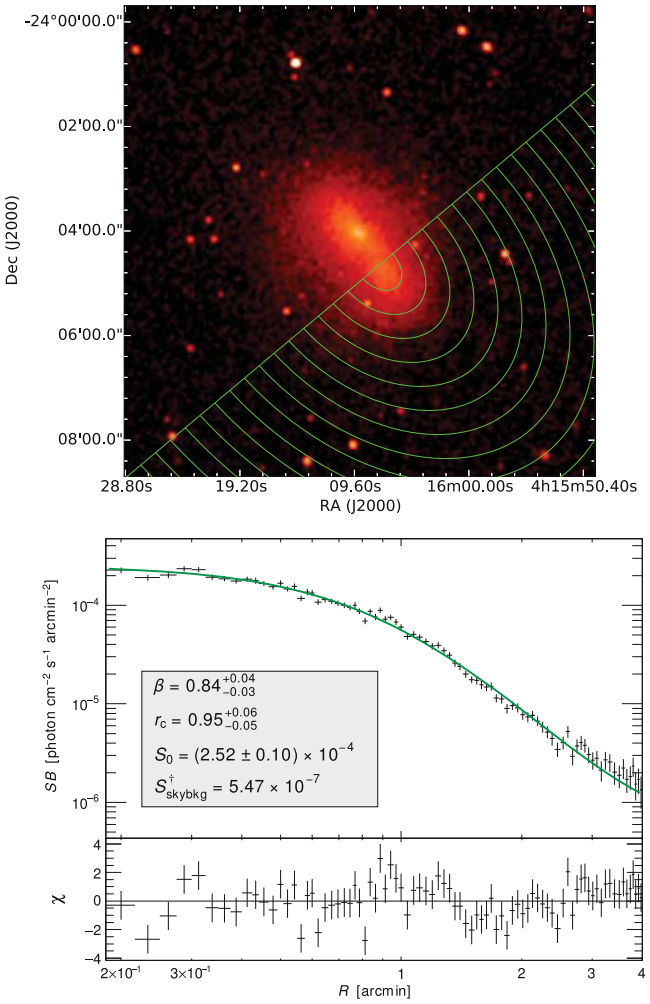

Figure 6. *Top:* Sector used to model the surface brightness of the SW subcluster. Annuli are drawn only to guide the eye and do not reflect the actual bin size used for the surface brightness profiles. *Bottom:* β-model fit to the surface brightness profile of the SW subcluster. For clarity, the profile shown in this plot was binned to have 200 counts per bin. The best-fitting model parameters are listed; radii units are arcmin, and surface brightness units are photon cm^{-2} s^{-1} arcmin^{-2}. Fixed parameters are shown with a superscripted †. The bottom panel shows the residuals of the fit.

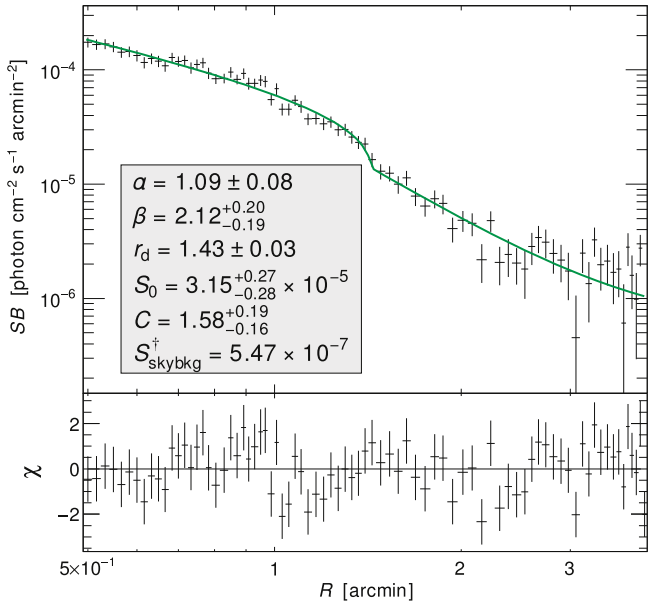

Figure 7. Broken power-law model fit to the surface brightness profile of the SW subcluster in a subsector with position angles 280°–340°, measured from the W in counterclockwise direction. For clarity, the profile shown in this plot was binned to have 80 counts per bin. The best-fitting model parameters are listed; radii units are arcmin, and surface brightness units are photon cm^{-2} s^{-1} arcmin^{-2}. Fixed parameters are shown with a superscripted †.

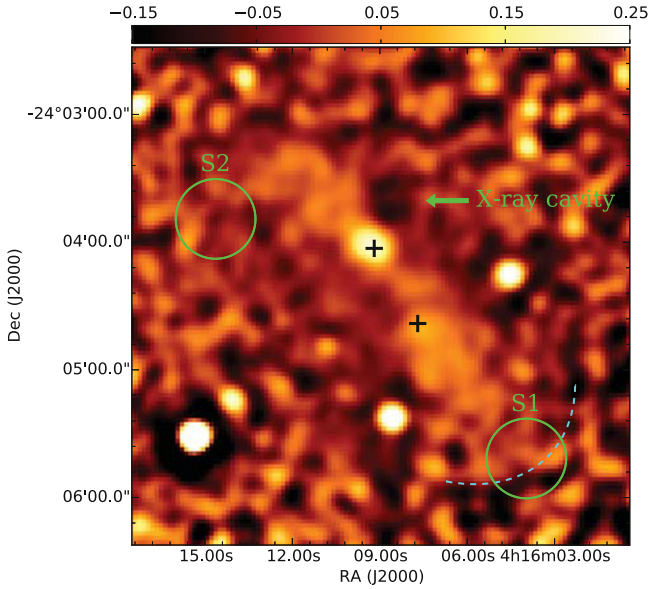

Figure 8. Unsharp-masked X-ray image of MACS J0416.1-2403, created by dividing the difference of two 0.5–4 keV fluxed images convolved with Gaussians of widths 4″ and 10″ by their sum. Point sources have not been subtracted from this image, and there are some residuals surrounding them. The positions of the two less massive mass structures identified by Jauzac et al. (2015) are marked as S1 and S2 with circles of diameters 100 kpc, as also done by Jauzac et al. (2015). Black crosses mark the centers of the DM halos of the two main subclusters (M. Jauzac 2015, private communication). The dashed arc shows the position of the density discontinuity detected near the SW subcluster. The location of the X-ray cavity is also marked.

associated with cD galaxies in the NE and SW subclusters. These sources are also detected in the GMRT 610 MHz image (Figure 11). These two point-like AGN have 1.5 GHz integrated flux densities[31] of 1.47 ± 0.08 (NE) and 0.27 ± 0.03 (SW) mJy. At 610 MHz we measure flux densities of 3.24 ± 0.34 (NE) and 0.33 ± 0.07 (SW) mJy for these sources. Using these fluxes, we compute spectral indices of $\alpha = -0.88 \pm 0.13$ (NE) and $\alpha = -0.22 \pm 0.27$ (SW), which are typical for AGN (e.g., Prandoni et al. 2009).

We also find diffuse extended emission in the cluster. The diffuse emission reveals itself in the JVLA image as an increase in the "noise" in the general cluster area. This diffuse emission is better visible in our low-resolution tapered image with emission from compact sources subtracted (Figure 10). The diffuse emission has a elongated shape measuring about 120″ × 45″ (0.65 by 0.24 Mpc) and is oriented along a NE-SW axis, following the overall distribution of the X-ray emission. We also find evidence for this diffuse emission in the

[31] The errors on the flux measurements include the absolute flux calibration uncertainty and the uncertainty based on the map noise, taking the integration area into account. The uncertainties were added in quadrature. For the JVLA, we assumed a 5% uncertainty for the absolute flux scale bootstrapped from the primary calibrator sources. For the GMRT observations, we assumed an uncertainty in the absolute flux scale of 10%.

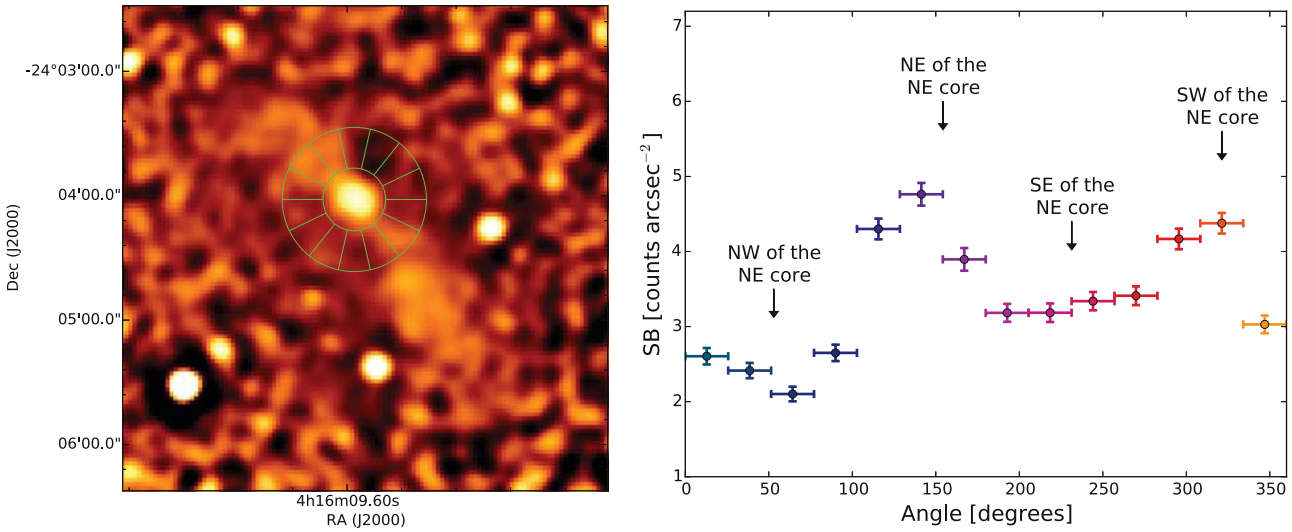

Figure 9. *Left:* Unsharp-masked image as in Figure 8, with overlaid partial annuli used to evaluate the azimuthal surface brighness profile around the NE core. *Right:* Azimuthal surface brightness profile around the NE core. The largest dip in the profile is in the direction of the cavity seen in the unsharp-masked image, between opening angles of 51°–77°. Angles are measured counterclockwise, starting from the W.

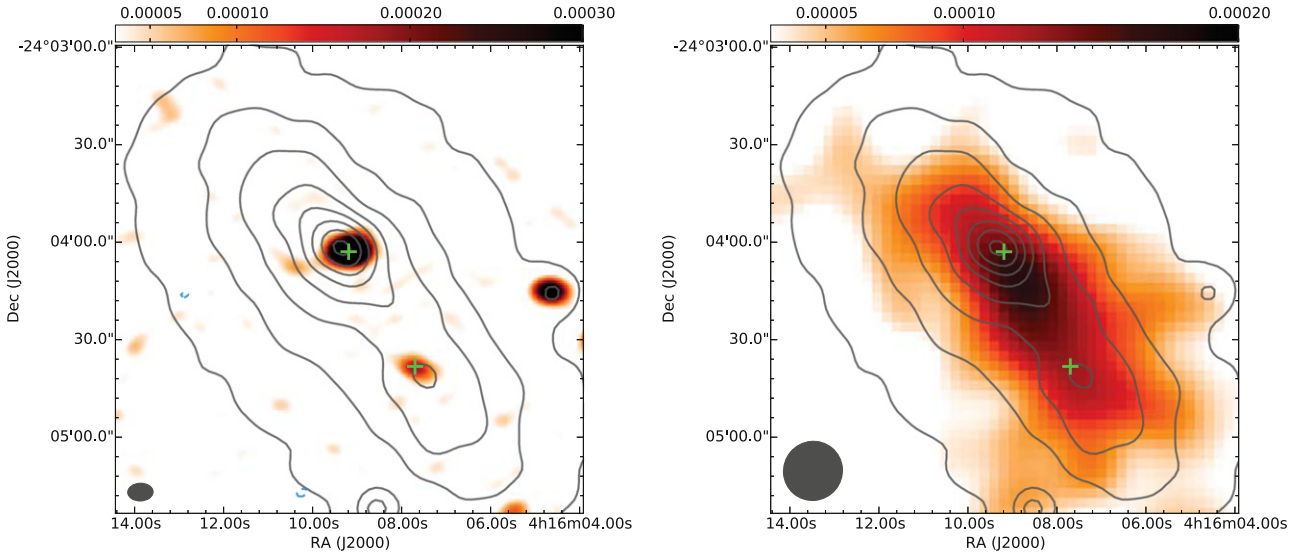

Figure 10. *Left:* JVLA 1–2 GHz high-resolution image showing the compact sources in the cluster region. *Right:* JVLA 1–2 GHz image of the radio halo, with compact sources subtracted. *Chandra* contours are overlaid on both images. The contours are based on an exposure-corrected, vignetting-corrected image that was smoothed with a Gaussian kernel of width 4″; they are drawn at [0.6, 1.3, 2.0, 2.7, …] × 10^{-7} photons cm^{-2} s^{-1}. Green crosses mark the centers of the DM halos. Dashed blue lines show the -3σ radio contours (these are only visible in the high-resolution radio image). The beam size is shown in the bottom left corner of the images.

GMRT 610 MHz image, although less clearly than in the JVLA 1.5 GHz image (Figure 11). In the low-resolution tapered GMRT image there is again evidence for diffuse emission, but the peak flux is only at a level of $3\sigma_{\rm rms}$.

For the integrated flux of the diffuse emission, we measure 1.60 ± 0.14 mJy (at 1.5 GHz) in an ellipse with radii of 70″ by 40″ oriented with a position angle of 45° (following the overall brightness distribution). From the GMRT tapered image, we estimate an integrated 610 MHz flux of 6.8 ± 3.0 mJy for the diffuse emission in the same area. We evaluated the accuracy of the compact source subtraction and conclude that this does not add significantly to the uncertainty on the radio halo flux. Based on the residuals visible for the brightest source in the field, we find that the compact source subtraction was performed at a level better than 0.5%.

Taking the two flux measurements at 1.5 and 0.61 GHz, we obtain a spectral index of $\alpha_{1500}^{610} = -1.6 \pm 0.5$ for the diffuse emission. Based on the above results, we compute a radio power of $P_{1.4\,\rm GHz} = (1.3 \pm 0.3) \times 10^{24}\,\rm W\,Hz^{-1}$, scaling with the spectral index of $\alpha = -1.6 \pm 0.5$.[32]

VLITE shows emission co-incident with the NE subcluster where the higher resolution 1–2 GHz images (Figure 10) reveal the compact sources and the brightest portion of the diffuse emission. We fit the 320–360 MHz VLITE emission with a single Gaussian component to measure the integrated flux. We measure a total flux of 20.5 ± 7.0 mJy, where we have included a 13% uncertainty in the source flux, as determined for a low

[32] We included the spectral index uncertainty in the uncertainty on the radio power.

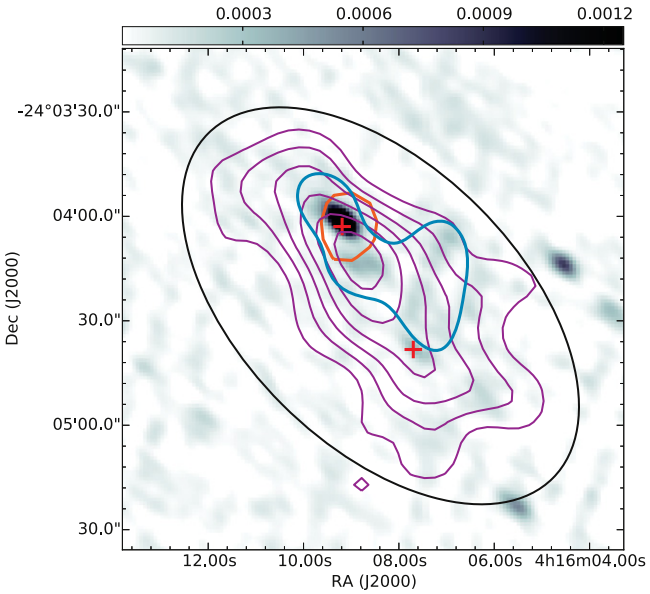

Figure 11. GMRT 610 MHz high-resolution image, showing the compact radio sources. Overlaid in blue are GMRT 610 MHz contours of the diffuse radio emission, drawn at 1.1 mJy/beam. JVLA 1–2 GHz radio contours showing diffuse radio emission are drawn in magenta at [60, 80, 100, 120, 140, 160] μJy/beam. VLITE 340 MHz radio contours are drawn in orange at 10 mJy/beam. The ellipse shows the region in which the radio flux was measured. Crosses mark the centers of the dark matter halos of the NE and SW subclusters.

signal-to-noise source in VLITE (Clarke et al. 2015, in preparation). The VLITE emission contains both the diffuse component and the compact emission from the two point sources associated with the NE and SW clusters. We use the VLA and GMRT flux measurements to determine the spectral index of the two compact sources, assume that spectral index extends to the central VLITE frequency, and estimate the contribution to the total VLITE emission from the compact sources. We subtract that from the VLITE flux and get an estimate of the diffuse component detected by VLITE of 14.6 $\pm$ 7.0 mJy. Comparing the VLITE flux to the JVLA flux, we calculate a spectral index of $\alpha_{1500}^{340} = -1.5 \pm 0.8$. The results are consistent with the spectral index estimate from the GMRT data. Deeper low-frequency data are required to better constrain the spectral properties of the diffuse emission.

In the JVLA 1–2 GHz data we did not detect diffuse polarized emission in the cluster in Stokes Q and U images we made. Halos are generally unpolarized at the few percent level or less so this result is not surprising (e.g., Feretti et al. 2012). We note however, that a proper search for diffuse emission, taking full advantage of the large bandwidth, would require Faraday Rotation Measure Synthesis.

[33] An analysis of the DM-gas offset in MACS J0416.1-2403 was carried out more recently by Harvey et al. (2015). For the SW subcluster, their DM peak is offset by about 100 kpc ($\sim$20″) from the DM peak determined by previous analyses (e.g., Grillo et al. 2015; Jauzac et al. 2015, models at https://archive.stsci.edu/pub/hlsp/frontier/macs0416/models/). We do not understand the cause of the offset, but choose to use the DM peaks determined by Jauzac et al. (2015), because their locations are consistent within 2″ with the locations of the DM peaks determined by other authors (e.g., Grillo et al. 2015). We also point out that the peak of the galaxy distribution chosen by Harvey et al. (2015) for the SW subcluster in MACS~J0416.1-2403 is strongly biased by a foreground galaxy ($z = 0.10^{+0.12}_{-0.08}$; Jouvel et al. 2014) at R.A. = 04: 16: 06.833 and decl. = −24: 05: 08.40 that was not excluded from their analysis.

9. GAS-DM DECOUPLING

The combined X-ray and lensing analysis of Jauzac et al. (2015) determined that the gas component of the SW subcluster has decoupled from the DM component and lags behind the subcluster's galaxies as it travels toward the NE subcluster. In the NE subcluster, on the other hand, the DM and gas components were determined by Jauzac et al. (2015) to spatially overlap.[33] Offsets between the DM and gas components of merging galaxy clusters set crucial constraints on the merger state. In particular, significant offsets indicate a post-merging system, while a lack of offsets supports a pre-merging scenario. Below, we discuss the DM-gas offsets in light of the deeper *Chandra* data.

The centers of the DM halos of the two subclusters (M. Jauzac 2015, private communication) are marked on Figure 12, which shows an *HST* ACS/F814W image of the cluster, with overlaid *Chandra* and JVLA contours. The centers of the X-ray cores were defined as the peaks in the X-ray emission, and were determined from the 0.5 to 4 keV *Chandra* surface brightness map of the cluster, convolved with a Gaussian of $\sigma = 4''$. We also considered the uncertainties on the surface brightness distribution, and defined the uncertainties on the X-ray peaks as the regions around the cores in which the X-ray brightness is consistent (within the propagated Poisson errors on the counts image) with the brightness of the corresponding peak. We note that our approach only provides a lower limit on the extent of the peak regions, because the background was included in the surface brightness map used for this analysis. The uncertainties on the DM centers are $<1''$, significantly smaller than the uncertainties on the centers of the X-ray cores. In Figure 13, we compare the position of the DM centers with that of the X-ray peak regions. Rather than confirming the previously-reported offset between the gas and DM components of the SW subcluster, Figure 13 shows that *both* X-ray peaks are, within the uncertainties, co-located with the DM centers. We speculate that the discrepancy between the results presented herein and those reported by Jauzac et al. (2015) is caused by a higher noise level in the significantly shallower X-ray data used in previous studies; our data is $\approx$6 times deeper, which is equivalent to a reduction in noise by a factor of $\approx$2.5.

10. MERGER SCENARIO

Jauzac et al. (2015) showed that the galaxy redshift distribution in MACS J0416.1-2403 is bimodal relative to the mean redshift, with the SW subcluster (mean redshift 0.3966) moving toward the observer and the NE subcluster (mean redshift 0.3990) moving away from the observer. Based on these observations, Jauzac et al. (2015) suggested two possible merger scenarios:

1. MACS J0416.1-2403 is a *pre-merging* system, in which the SW subcluster comes from behind the NE subcluster, and is now seen near first core passage;
2. MACS J0416.1-2403 is a *post-merging* system, in which the SW cluster approached the NE subcluster from above, and is now seen near its second core passage.

We refer the reader to Figure 13 of Jauzac et al. (2015) for a sketch of the two geometries. In this section, we try to distinguish between the two scenariosusing our X-ray and radio findings.

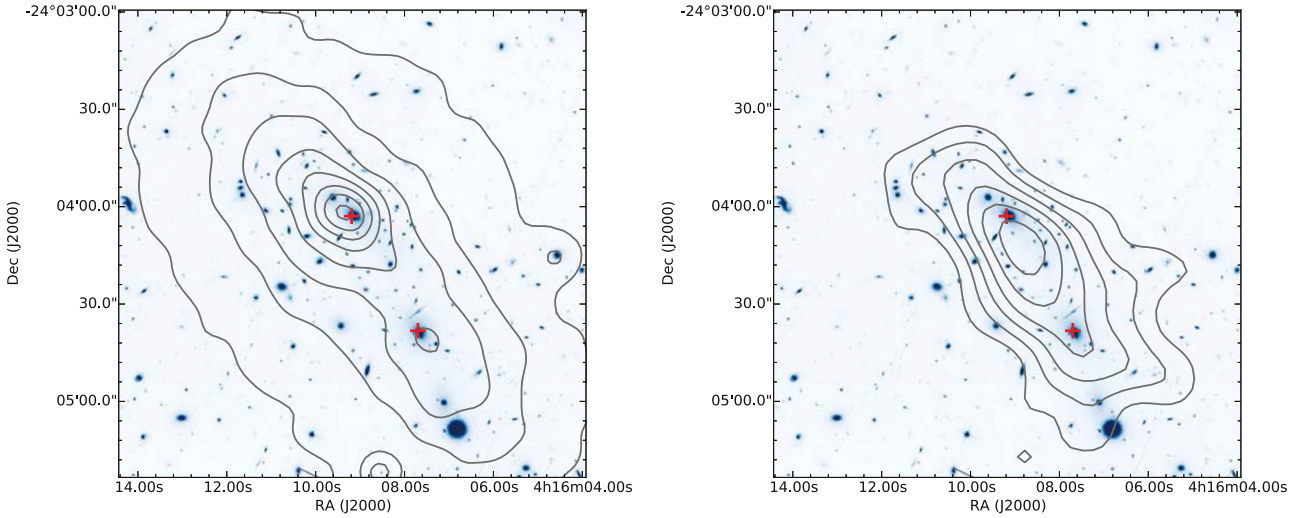

Figure 12. *HST* ACS/F814W optical image of MACS J0416, with overlaid *Chandra* (left) and JVLA (right) contours. X-ray contours are the same as in Figure 10. Radio contours are based on the JVLA image with the emission from compact sources subtracted using a Gaussian uv-taper of 20″. The JVLA contours are drawn at [60, 80, 100, 120, 140, 160] μJ/beam. The centers of the DM halos of the NE and SW subclusters are marked with red crosses.

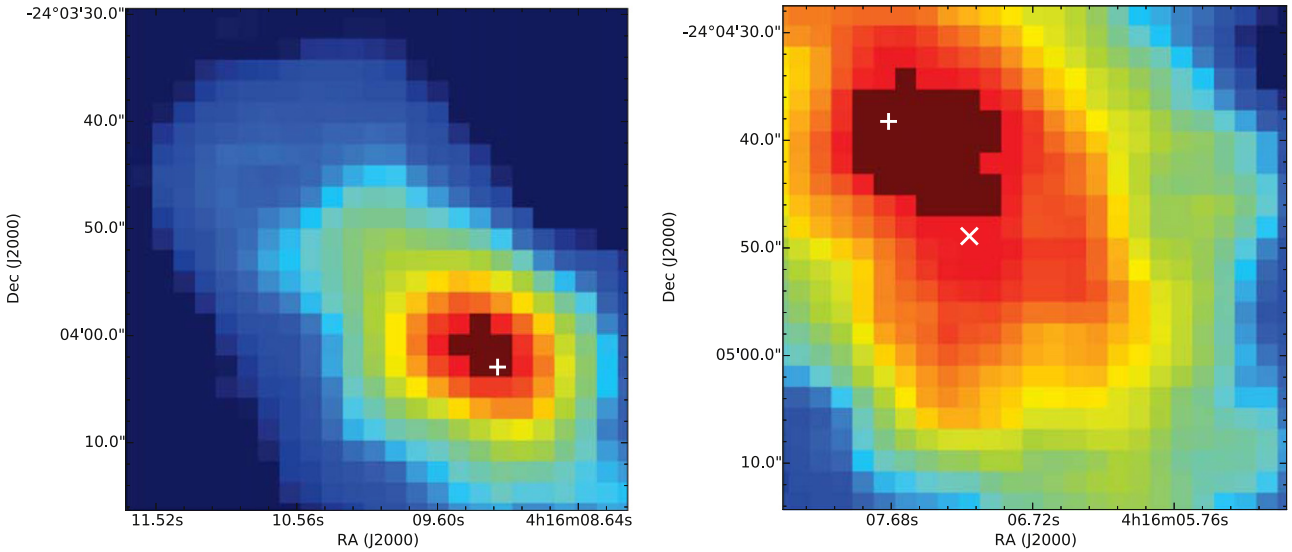

Figure 13. *Chandra* 0.5–4 keV surface brightness maps of the NE subcluster center (left) and of the SW subcluster center (right). The overexposed regions (in brown) are the peak regions of the two subcluster cores. The position of the DM centers are marked with white crosses. The white "X" indicates the location of the X-ray peak of the SW subcluster, as it was identified from shallower *Chandra* data by Jauzac et al. (2015).

10.1. Cooler Gas in the NE?

Approximately 300 kpc NE of the NE core, the temperature maps show a region (region #10; $T = 8.41^{+1.37}_{-0.90}$ keV) that is cooler than the neighboring region closer to the cluster center (region #8; $T = 12.18^{+2.41}_{-1.90}$). The cool gas in this region could be pre-shock gas ahead of a shock front. We examined the surface brightness profile across the cooler region, but could not confirm a surface brightness discontinuity with a confidence $\geqslant$90%. A density jump could be masked by projection effects. Nonetheless, while the temperature difference between regions #8 and #10 is significant at 90% confidence (but not at 2σ) and there is a pseudo-pressure jump between the two regions, the lack of a clear density jump does not allow us to confirm a shock front NE of the NE core.

10.2. No Gas-DM offset

In head-on binary mergers, the essentially collisionless DM travels ahead of the collisional gas. There are several scenarios that could explain the spatial overlap of the DM andthe gas in MACS J0416.1-2403:

(i) In MACS J0416.1-2403, the NE and SW subclusters are seen before first core passage and have yet to interact strongly with each other (e.g., due to the subclusters still being very far apart, and/or to the merger having a high impact parameter). This scenario requires that the merger axis is significantly inclined with respect to the plane of the sky, because, in projection, the distance between the subcluster cores is only $\sim$250 kpc.

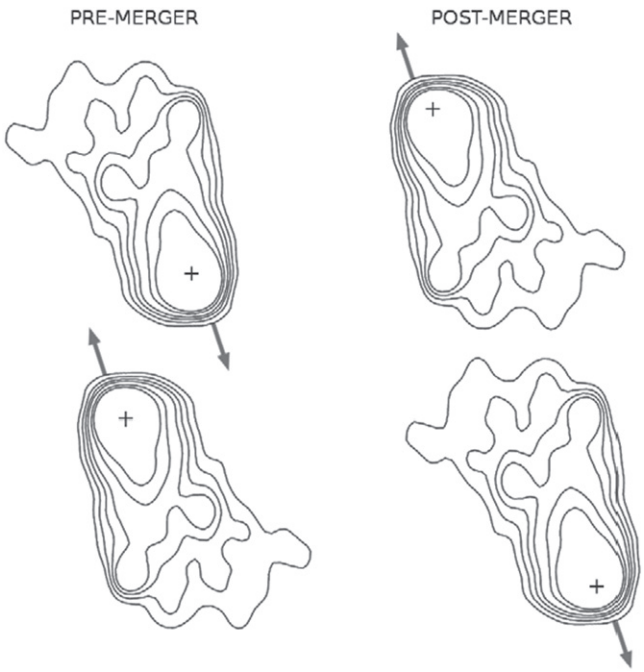

Figure 14. Effects of ram pressure on the morphologies of two merging clusters before first core passage (left) and after first core passage (right). The contours used in the sketch are based on the *XMM-Newton* surface brightness map of the group NGC 4839 infalling onto the Coma cluster.

(ii) The DM and gas in the NE and SW subclusters overlap only in projection. This requires either that one of the subclusters was essentially undisturbed by the merger and our line of sight aligns with the trajectory of the other subcluster, or that the subclusters' trajectories are parallel and both are aligned with our line of sight.

(iii) The NE and SW subclusters are seen after first core passage, and the gas of the SW subcluster slingshot and caught up with the DM halo, after they had separated near pericenter.

The radial velocity difference between the BCGs of the NE and SW subclusters was reported by Jauzac et al. (2015) to be $\approx$800 km s^{-1}. The sound speed in a cluster with a temperature of $\approx$10 keV is $\approx$1300 km s^{-1}, and typical collision velocities are 1–2 times the sound speed. Therefore, the radial velocity difference between the two BCGs in MACS J0416.1-2403 seems rather low compared to typical collision velocities, and supports a scenario in which the merger progresses outside the plane of the sky, but the merger axis is not perpendicular to the plane of the sky. Alternatively, the merger could be seen after first core passage, near the turnaround point; this scenario requires a merger axis that is almost perpendicular to the plane of the sky.

10.3. Subcluster Morphology

The effects of ram pressure on the morphologies of two merging clusters also provide clues on the merger scenario. When two clusters merge, tails that trail the cluster cores may form. In a post-merging system seen before turnaround, these plasma tails are elongated toward the core of the opposite subcluster core. In a pre-merging system, the tails are elongated away from the opposite subcluster core. The two morphologies are sketched in Figure 14. In MACS J0416.1-2403, tails are not immediately seen in the surface brightness map. However, the unsharp-masked image in Figure 8 reveals that both the NE and the SW subclusters are trailed by tails whose directions are consistent with a pre-merger scenario.

10.4. Substructure in the NE Core

The surface brightness profile of the NE subcluster cannot be described by a single β-model, but instead by a double β-model composed of a very compact core and a more extended gas halo. Such a profile is typically used to model cool core clusters (e.g., Jones & Forman 1984; Ota et al. 2013), but it can also describe the surface brightness of merging clusters seen in projection (e.g., Zuhone 2009; Machacek et al. 2010). The core of the NE subcluster is very hot and has a long cooling time, which disfavors the possibility that the NE subcluster hosts a cool core. Instead, the observed substructure is more likely the result of a merger event.

The most straight-forward scenario would be that the NE and SW subclusters have already merged, and while the core of the SW subcluster was destroyed in the collision, as evidenced by the subcluster's flat surface brightness, the core of the NE subcluster survived. Cool cores that survive a recent merger event preserve part of their cold gas. However, we found no evidence of cool gas in the NE core. Therefore, the NE core is unlikely to be the remnant of a recent interaction between the NE and SW subclusters.

An alternative scenario is that the NE subcluster is merging with the DM halo S2 (Figure 8). However, S2 is not associated with a concentration of galaxies, and thus is an unlikely candidate for a group of galaxies (Jauzac et al. 2015). No other mass concentration that the NE subcluster might be currently merging with has been detected.

One other possibility, postulated by numerical simulations of Poole et al. (2008), is that the NE subcluster underwent a merger or a series of mergers over $\sim$1 Gyr ago, and while its core has already relaxed back to a compact state, it has not yet recooled. In this scenario, the merger could not have been with the SW subcluster, because the two subclusters are involved in an ongoing merger. Instead, the NE subcluster needs to have interacted several Gyr ago with one or more clusters that are no longer directly detectable in the X-ray maps, in the lensing maps, or in the redshift distribution of the NE subcluster.

Alternatively, past mergers could also have heated the cool core without destroying it, by inducing sloshing in the central galaxy. The kinetic energy of the sloshing central galaxy would then have been dissipated as heat between successive mergers (ZuHone et al. 2010).

10.5. The AGN and the X-Ray Cavity in the NE Core

The collision velocity between the NE and SW subcluster is unlikely to be highly supersonic. If the cluster is a post-merging system, a cavity could have had enough time to form since first core passage. However, given the short timescale and the intense turbulence following the moment of first core passage, forming a new cavity would require a strong AGN outburst. The expectation would then be to observe radio emission associated with the X-ray cavity. However, this radio emission is not observed. Instead, the presence of an X-ray cavity NW of the NE core supports a pre-merger scenario. The cavity was most likely inflated by a recent weak outburst of the AGN detected in the BCG of the NE subcluster.

10.6. SW Density Discontinuity

The density discontinuity detected S of the SW subcluster is located along the line connecting the NE subcluster, the SW subcluster, and S1. The discontinuity also appears coincident with the position of S1, but this could be a projection effect. There are two scenarios that would explain the origin of the density discontinuity: the merger of the SW subcluster with S1, or the merger of the SW subcluster with the NE subcluster.

If the discontinuity were triggered by a merger between the two main subclusters, then the merger must have already progressed past the moment of the first core passage. Furthermore, because the NE core is very compact and hosts an X-ray cavity, it is unlikely that it was significantly affected by a merger with the SW subcluster. Therefore, taking into account the constraints set by the lack of an offset between the gas and DM peaks of both subclusters, it is the SW subcluster whose trajectory must be aligned with our line of sight. In this geometry, a shock front would be expected ahead of the SW subcluster (with respect to its direction of motion), i.e., our line of sight should be perpendicular to the 3D shock "cap." Instead, however, the surface brightness discontinuity we detect is seen in projection only S-SW of the SW subcluster. If the detected density discontinuity is the appearance of the shock in projection, then we would expect to observe it over a larger angular opening. Most likely, the density discontinuity is caused by the interaction of the SW subcluster with S1.

In conclusion, while we cannot completely eliminate the possibility of MACS J0416.1-2403 being a post-merging cluster, we believe *the sum of our findings favors a pre-merging scenario*.

11. A NEWLY DISCOVERED RADIO HALO

We classify the diffuse radio emission in the cluster as a halo, since the emission has low-surface brightness, large extent, and is centrally located. With a largest linear size (LLS) of 0.65 Mpc, the halo has a somewhat smaller size than other radio halos in merging clusters, which have LSSs of 1–1.5 Mpc. (e.g., Feretti et al. 2012). However, the LLS is larger than that of the radio mini-halos found in cool core clusters (e.g., Burns et al. 1992; Gitti et al. 2007; Giacintucci et al. 2014). Additionally, an important difference from mini-halos is that neither the NE nor the SW subclusters contains a cool core.Furthermore, as shown in Figure 12, the halo seems to be associated with both subclusters. The halo in MACS J0416.1-2403 is also rather elongated compared to most known radio halos. However, there are other clusters with similarly elongated radio halos (e.g., Bonafede et al. 2012; van Weeren et al. 2012a, 2012b; Shimwell et al. 2014).

The radio emission around the northern subcluster contains about a factor of 2 more flux than the emission around the southern one. An interesting question is whether we observe a single radio halo, caused by the merger between the NE and the SW subclusters, or two individual halos belonging to the two subclusters. In the latter case, these halos must have originated from previous merger events within two subclusters themselves. This would make MACS J0416.1-2403 similar to the case of the radio halo pair in Abell 399 and Abell 401 (Murgia et al. 2010), with the difference that Abell 399/401 seems to be at a much earlier pre-merger stage.

For radio halos, a correlation is observed between the cluster's X-ray luminosity and the radio halo power (the L_X–P correlation), with the most X-ray luminous clusters corresponding to the most powerful radio halos (e.g., Liang et al. 2000; Enßlin & Röttgering 2002; Cassano et al. 2006). The X-ray luminosity is used as a proxy of cluster mass. The distribution in the L_X–P plane is bimodal when clusters without halos are included. Merging clusters with radio halos follow the L_X–P correlation, while the upper limits on the radio power of other clusters are well below the correlation (Brunetti et al. 2007).

A correlation is also observed between the cluster's integrated Sunyaev–Zel'dovich (SZ) effect (i.e., the integrated Compton Y_{SZ} parameter) and the radio halo power (e.g., Basu 2012, 2013). Y_{SZ} is proportional to the volume integral of the pressure. The SZ signal should be less affected by the cluster dynamical state and therefore is expected to be a better indicator of the cluster's mass. Basu (2012, 2013) and Cassano et al. (2013) showed that there is good agreement between the $Y_{SZ}-P$ scaling relation and the scaling relations based on X-ray data.

In Figure 15, we place MACS J0416.1-2403 on the L_X–P and Y_{SZ}–P diagrams, with the values for the other clusters taken from Cassano et al. (2013). The $Y_{SZ,500}$ value for the cluster was recently calculated by Planck Collaboration et al. (2015), which found $Y_{SZ,500} = (0.71 \pm 0.24) \times 10^{-4}$ Mpc^2. Specifically, this is the value of $Y_{SZ,500}$ obtained from the union catalog based on the MMF1[34] detection algorithm. We also computed the value of $Y_{SZ,500}$ using the gNFW model fit to Bolocam presented by Czakon et al. (2015) and obtained $Y_{SZ,500} = (1.49 \pm 0.28) \times 10^{-4}$ Mpc^2. The difference between the Planck and Bolocam measurements is not understood, but is likely due to some combination of random noise fluctuations, deviations from the assumed pressure profile used to extract $Y_{SZ,500}$ (particularly at large radii), contamination from dust or other astronomical signals, and calibration uncertainties. Furthermore, we note that this cluster is not detected by PowellSnakes—one of the three Planck algorithms—and the values of $Y_{SZ,500}$ obtained from the other two algorithms (MMF1 and MMF3[35]) are significantly different, perhaps indicating that measurements of $Y_{SZ,500}$ toward this cluster contain larger than typical systematic uncertainties. In Figure 15, we plot both the Planck and Bolocam values of $Y_{SZ,500}$.

Interestingly, the radio halo power falls on the low end of the L_X–P correlationfor radio halos without ultra-steep spectra. However, using the Planck measurement of $Y_{SZ,500}$, we find that the halo power is consistent with the expected Y_{SZ}–P correlation, indicating the halo is not underluminous for the cluster mass. While the Bolocam value of $Y_{SZ,500}$ does imply lower than expected halo power, the nominal Y_{SZ}–P relation used for comparison is derived solely from Planck SZ measurements. We therefore consider our interpretation based on the Planck value of $Y_{SZ,500}$ to be more robust. Given this interpretation, MACS J0416.1-2403 could be just an outlier in the L_X–P diagram, based on the fact that there is significant scatter in the correlations.

It is also possible that the X-ray luminosity of MACS J0416.1-2403 is not a good indicator of the cluster's mass, and the luminosity is boosted by the merger. A boost in X-ray luminosity is predicted for approximately one sound-crossing time, which for MACS J0416.1-2403 is $\approx$1 Gyr (Ricker & Sarazin 2001). This boost would affect other clusters on the

[34] Matched multi-filter algorithm, implementation 1.
[35] Matched multi-filter algorithm, implementation 3.

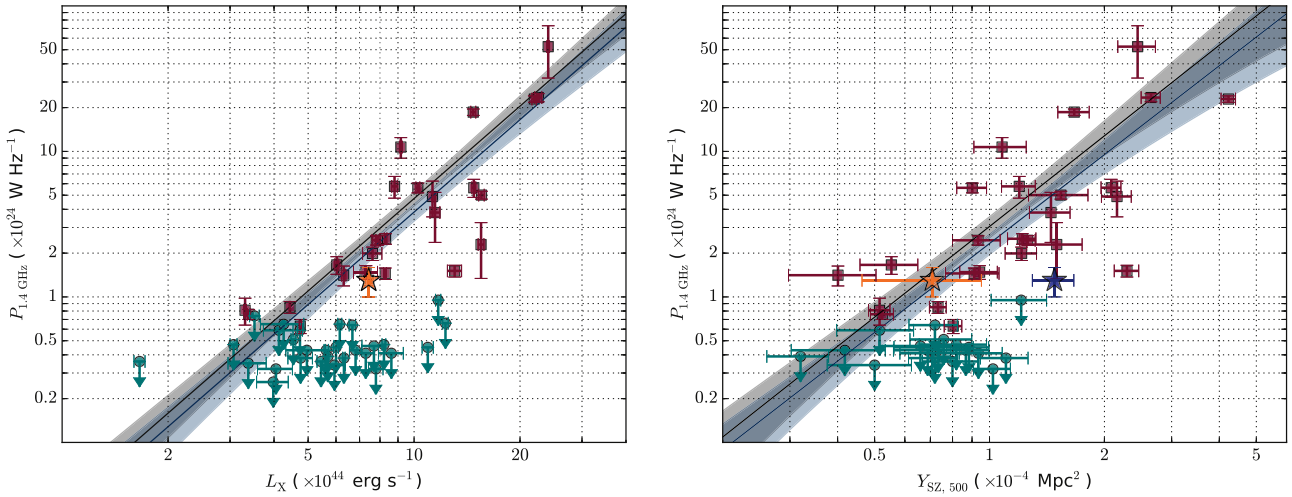

Figure 15. L_X–P and Y_{SZ}–P diagrams. Clusters with only upper limits on the radio halo power are shown in teal-colored circles, while clusters with detected halos are shown in dark red squares. On both diagrams, MACS J0416.1-2403 is represented with a star. In the Y_{SZ}–P diagram, the orange star corresponds to the $Y_{SZ,500}$ value reported by Planck Collaboration et al. (2015), while the blue star corresponds to the $Y_{SZ,500}$ value calculated from the gNFW fit to Bolocam presented in Czakon et al. (2015). Error bars are drawn for all points, but some are very small and barely visible. Values for all clusters with the exception of MACS J0416.1-2403 are taken from Cassano et al. (2013). Power-laws show the best-fitting L_X–P and Y_{SZ}–P correlations for radio halos with $\alpha > -1.5$ (black) and for all known radio halos (including ultra-steep spectrum halos; dark blue). Gray and light blue areas indicate the 95% confidence regions of the correlations. An interactive version of the diagrams is available at http://hea-www.cfa.harvard.edu/~gogrean/Lx-P.html.

correlation as well, but it could affect MACS J0416.1-2403 more since we are seeing a cluster close to first core passage. The mass of the cluster in R_{500} is $(7.0 \pm 1.3) \times 10^{14}\,M_\odot$ (Umetsu et al. 2014). Based on the scaling relations of Pratt et al. (2009), the mass corresponds to a 0.1–2.4 keV cluster luminosity of $(1.1 \pm 0.4) \times 10^{45}$ erg s^{-1}, which is in agreement with the luminosity calculated from the *Chandra* data. Therefore, based on the M_{500}–L_{500} scaling relation, we have no indication that the cluster luminosity is higher than expected for a cluster of this mass.

Another possibility is that we are seeing an ultra-steep spectrum radio halo ($\alpha \lesssim -1.5$, Brunetti et al. 2008). In this case, the radio halo is only underluminous at higher frequencies (i.e., above a GHz), while the integrated flux density rapidly increases at lower frequencies. Ultra-steep spectrum radio halos are predicted by the turbulent re-acceleration model to form in less energetic mergers (Brunetti et al. 2008). The mass of MACS J0416.1-2403 is indeed near the lower end of the mass range of clusters with radio halos (see, e.g., Cassano et al. 2013, who list masses between $4.4 \times 10^{14}\ M_\odot$ and $1.7 \times 10^{15}\ M_\odot$ for clusters hosting radio halos). Some, but not all clusters with masses similar to that of MACS J0416.1-2403 host ultra-steep spectrum radio halos. The steepness of the radio spectrum is affected not only by the cluster mass though, but also by the magnetic fields of the clusters and by the particle acceleration efficiency; at the moment, these are not known.

An ultra-steep spectrum radio halo is also expected in the later phases of a merger, when the radio spectrum had time to steepen due to synchrotron and IC losses (e.g., Donnert et al. 2013). If the diffuse radio emission in MACS J0416.1-2403 is ultra-steep and the steepness was caused by ageing, then the emission in the cluster is in fact consisting of two individual radio halos that were formed in the NE and SW subclusters during previous mergers—possibly the same mergers that heated the cluster cores.

Unfortunately, the 320–360 MHz VLITE and 610 MHz GMRT data presented in Section 8 are not sufficient to confirm, or rule out, the presence of an ultra-steep spectrum radio halo. Low-frequency GMRT ($\nu < 610$ MHz) and/or deep P-band JVLA observations are required to settle this case.

A third possibility is that we could be witnessing the first stages of the formation of this radio halo. We do not think that the radio halo is fading, because the NE and SW subclusters are still in the process of merging and most likely they have not yet undergone core passage (see Section 10). Therefore, when the merger progresses further, the radio halo could brighten, increase in size, and move onto the correlation.

12. SUMMARY

The *HST* Frontier Field cluster MACS J0416.1-2403 ($z = 0.396$) is a merging system that consists of two main subclusters and two additional smaller mass structures (Jauzac et al. 2015). Here, we presented results from deep *Chandra* JVLA, and GMRT observations of the cluster. The main aims of our analysis were to identify signatures of merger activity in the ICM, constrain the merger scenario, and detect and characterize diffuse radio sources. Below is a summary of our main findings:

1. The cluster has an average temperature of $10.06^{+0.50}_{-0.49}$ keV, an average metallicity of $0.24^{+0.05}_{-0.04}\ Z_\odot$, and a 0.1–2.4 keV luminosity of $L_X = (7.43 \pm 0.08) \times 10^{44}$ erg s^{-1}.
2. The NE subcluster has a very compact core and a nearby X-ray cavity, but its temperature is very high ($T \sim 10$ keV), we find no evidence of multi-phase gas, and its cooling time is $\gtrsim$3 Gyr. The presence of a compact core and of an X-ray cavity indicates that the NE subcluster was not disrupted by a recent major merger event.
3. S-SW of the SW subcluster, there is a weak density discontinuity that is best-fitted by a density compression of $1.56^{+0.38}_{-0.29}$. The discontinuity is located along the line connecting the NE subcluster, the SW subcluster, and the mass structure S1 reported by Jauzac et al. (2015). Most likely, the discontinuity was caused by a collision

between the SW subcluster and S1, rather than by a collision between the NE and SW subclusters.

4. The DM and gas components of the NE and SW subclusters are well-aligned, which favors a scenario in which the two subclusters are seen before first core passage.
5. MACS J0416.1-2403 has a radio halo with a 1.4 GHz power of $(1.3 \pm 0.3) \times 10^{24}$ W Hz^{-1}, which is somewhat less luminous than predicted by the L_X–P correlationfor radio halos without ultra-steep spectra. However, the halo aligns well on the $Y_{SZ,500}$–P correlation, indicating that it is not underluminous for the cluster mass.We could be observing the birth of a giant halo, or a very rare ultra-steep halo.

We thank the referee for constructive comments. We also thank Mathilde Jauzac for providing the coordinates of the centers of the DM halos, and Becky Canning and Aurora Simionescu for constructive discussions.

G.A.O. acknowledges support by NASA through a Hubble Fellowship grant HST-HF2-51345.001-A awarded by the Space Telescope Science Institute, which is operated by the Association of Universities for Research in Astronomy, Incorporated, under NASA contract NAS5-26555. R.J.vW. is supported by NASA through the Einstein Postdoctoral grant number PF2-130104 awarded by the *Chandra* X-ray Center, which is operated by the Smithsonian Astrophysical Observatory for NASA, under contract NAS8-03060. A.Z. acknowledges support by NASA through a Hubble Fellowship grant HST-HF2-51334.001-A awarded by the Space Telescope Science Institute, which is operated by the Association of Universities for Research in Astronomy, Incorporated, under NASA contract NAS5-26555. This research was performed while T.M. held a National Research Council Research Associateship Award at the Naval Research Laboratory (NRL). Basic research in radio astronomy at NRL by T.M. and T.E.C. is supported by 6.1 Base funding. F.A.S. acknowledges support from *Chandra* grant G03-14131X.

The scientific results reported in this article are based on observations made by the *Chandra* X-ray Observatory. Part of the reported results are based on observations made with the NASA/ESA *Hubble Space Telescope*, obtained from the Data Archive at the Space Telescope Science Institute, which is operated by the Association of Universities for Research in Astronomy, Inc., under NASA contract NAS 5-26555. The *HST* observations are associated with program #13496. The National Radio Astronomy Observatory is a facility of the National Science Foundation operated under cooperative agreement by Associated Universities, Inc. We thank the staff of the GMRT that made these observations possible. The GMRT is run by the National Centre for Radio Astrophysics of the Tata Institute of Fundamental Research.

This research has made use of NASA's Astrophysics Data System, and of the NASA/IPAC Extragalactic Database (NED) which is operated by the Jet Propulsion Laboratory, California Institute of Technology, under contract with the National Aeronautics and Space Administration. Some of the cosmological parameters in this paper were calculated using Ned Wright's cosmology calculator (Wright 2006). This research made use of APLpy, an open-source plotting package for Python hosted at http://aplpy.github.com.

Facilities: CXO (ACIS), *HST* (ACS).

REFERENCES

Ackermann, M., Ajello, M., Atwood, W. B., et al. 2010, PhRvD, 82, 092003
Anders, E., & Grevesse, N. 1989, GeCoA, 53, 197
Basu, K. 2012, MNRAS, 421, L112
Basu, K. 2013, AN, 334, 350
Blasi, P., & Colafrancesco, S. 1999, APh, 12, 169
Bonafede, A. 2010, PhD thesis, Universita degli Studi di Bologna
Bonafede, A., Brüggen, M., van Weeren, R., et al. 2012, MNRAS, 426, 40
Briggs, E. L. 1995, PhD thesis, North Carolina State Univ.
Brunetti, G., & Blasi, P. 2005, MNRAS, 363, 1173
Brunetti, G., Giacintucci, S., Cassano, R., et al. 2008, Natur, 455, 944
Brunetti, G., & Jones, T. W. 2014, IJMPD, 23, 30007
Brunetti, G., & Lazarian, A. 2011, MNRAS, 412, 817
Brunetti, G., Setti, G., Feretti, L., & Giovannini, G. 2001, MNRAS, 320, 365
Brunetti, G., Venturi, T., Dallacasa, D., et al. 2007, ApJL, 670, L5
Burns, J. O., Sulkanen, M. E., Gisler, G. R., & Perley, R. A. 1992, ApJL, 388, L49
Cash, W. 1979, ApJ, 228, 939
Cassano, R., Brunetti, G., & Setti, G. 2006, MNRAS, 369, 1577
Cassano, R., Ettori, S., Brunetti, G., et al. 2013, ApJ, 777, 141
Cavaliere, A., & Fusco-Femiano, R. 1976, A&A, 49, 137
Cavaliere, A., & Fusco-Femiano, R. 1978, A&A, 70, 677
Chung, S. M., Gonzalez, A. H., Clowe, D., Markevitch, M., & Zaritsky, D. 2010, ApJ, 725, 1536
Churazov, E., Forman, W., Jones, C., & Böhringer, H. 2003, ApJ, 590, 225
Clarke, T. E., Kassim, N. E., Hicks, B. C., et al. 2011, MmSAI, 82, 664
Clowe, D., Bradač, M., Gonzalez, A. H., et al. 2006, ApJL, 648, L109
Cornwell, T. J. 2008, ISTSP, 2, 793
Cornwell, T. J., Golap, K., & Bhatnagar, S. 2005, in ASP Conf. Ser. 347, Astronomical Data Analysis Software and Systems XIV, ed. P. Shopbell, M. Britton, & R. Ebert (San Francisco, CA: ASP), 86
Cornwell, T. J., Golap, K., & Bhatnagar, S. 2008, ISTSP, 2, 647
Cotton, W. D. 2008, PASP, 120, 439
Czakon, N. G., Sayers, J., Mantz, A., et al. 2015, ApJ, 806, 18
Dawson, W. A., Wittman, D., Jee, M. J., et al. 2012, ApJL, 747, L42
De Luca, A., & Molendi, S. 2004, A&A, 419, 837
Deller, A. T., Brisken, W. F., Phillips, C. J., et al. 2011, PASP, 123, 275
Dolag, K., & Enßlin, T. A. 2000, A&A, 362, 151
Donnert, J., Dolag, K., Brunetti, G., & Cassano, R. 2013, MNRAS, 429, 3564
Ebeling, H., Edge, A. C., & Henry, J. P. 2001, ApJ, 553, 668
Eckert, D., Molendi, S., & Paltani, S. 2011, A&A, 526, A79
Elvis, M., Plummer, D., Schachter, J., & Fabbiano, G. 1992, ApJS, 80, 257
Enßlin, T. A., & Röttgering, H. 2002, A&A, 396, 83
Ettori, S. 2000a, MNRAS, 318, 1041
Ettori, S. 2000b, MNRAS, 311, 313
Feretti, L., Giovannini, G., Govoni, F., & Murgia, M. 2012, A&ARv, 20, 54
Giacintucci, S., Markevitch, M., Venturi, T., et al. 2014, ApJ, 781, 9
Gitti, M., Ferrari, C., Domainko, W., Feretti, L., & Schindler, S. 2007, A&A, 470, L25
Grillo, C., Suyu, S. H., Rosati, P., et al. 2015, ApJ, 800, 38
Harvey, D., Massey, R., Kitching, T., Taylor, A., & Tittley, E. 2015, Sci, 347, 1462
Henley, D. B., Shelton, R. L., Kwak, K., Joung, M. R., & Mac Low, M.-M. 2010, ApJ, 723, 935
Jauzac, M., Clément, B., Limousin, M., et al. 2014, MNRAS, 443, 1549
Jauzac, M., Jullo, E., Eckert, D., et al. 2015, MNRAS, 446, 4132
Jeltema, T. E., & Profumo, S. 2011, ApJ, 728, 53
Jones, C., & Forman, W. 1984, ApJ, 276, 38
Jouvel, S., Host, O., Lahav, O., et al. 2014, A&A, 562, A86
Kalberla, P. M. W., Burton, W. B., Hartmann, D., et al. 2005, A&A, 440, 775
Lage, C., & Farrar, G. 2014, ApJ, 787, 144
Liang, H., Hunstead, R. W., Birkinshaw, M., & Andreani, P. 2000, ApJ, 544, 686
Machacek, M. E., O'Sullivan, E., Randall, S. W., Jones, C., & Forman, W. R. 2010, ApJ, 711, 1316
Mann, A. W., & Ebeling, H. 2012, MNRAS, 420, 2120
Markevitch, M., Gonzalez, A. H., Clowe, D., et al. 2004, ApJ, 606, 819
Markevitch, M., Gonzalez, A. H., David, L., et al. 2002, ApJL, 567, L27
Markevitch, M., & Vikhlinin, A. 2007, PhR, 443, 1
McMullin, J. P., Waters, B., Schiebel, D., Young, W., & Golap, K. 2007, in ASP Conf. Ser. 376, Astronomical Data Analysis Software and Systems XVI, ed. R. A. Shaw, F. Hill & D. J. Bell (San Francisco, CA: ASP), 127
Merten, J., Coe, D., Dupke, R., et al. 2011, MNRAS, 417, 333
Mohan, N., & Rafferty, D. 2015, ascl:1502.007
Moretti, A., Campana, S., Lazzati, D., & Tagliaferri, G. 2003, ApJ, 588, 696

Murgia, M., Govoni, F., Feretti, L., & Giovannini, G. 2010, A&A, 509, A86
Offringa, A. R., de Bruyn, A. G., Biehl, M., et al. 2010, MNRAS, 405, 155
Ota, N., Onzuka, K., & Masai, K. 2013, PASJ, 65, 47
Owers, M. S., Nulsen, P. E. J., Couch, W. J., & Markevitch, M. 2009, ApJ, 704, 1349
Petrosian, V. 2001, ApJ, 557, 560
Planck Collaboration, Ade, P. A. R., Aghanim, N., et al. 2015, arXiv:1502.01598
Poole, G. B., Babul, A., McCarthy, I. G., Sanderson, A. J. R., & Fardal, M. A. 2008, MNRAS, 391, 1163
Prandoni, I., Morganti, R., & Mignano, A. 2009, arXiv:0909.3761
Pratt, G. W., Croston, J. H., Arnaud, M., & Böhringer, H. 2009, A&A, 498, 361
Randall, S., Nulsen, P., Forman, W. R., et al. 2008a, ApJ, 688, 208
Randall, S. W., Markevitch, M., Clowe, D., Gonzalez, A. H., & Bradač, M. 2008b, ApJ, 679, 1173
Rau, U., & Cornwell, T. J. 2011, A&A, 532, A71
Ricker, P. M., & Sarazin, C. L. 2001, ApJ, 561, 621
Sanders, J. S. 2006, MNRAS, 371, 829
Sayers, J., Czakon, N. G., Mantz, A., et al. 2013, ApJ, 768, 177
Schirmer, M., Carrasco, R., Pessev, P., et al. 2015, ApJS, 217, 33
Shimwell, T. W., Brown, S., Feain, I. J., et al. 2014, MNRAS, 440, 2901
Shimwell, T. W., Markevitch, M., Brown, S., et al. 2015, MNRAS, 449, 1486
Snowden, S. L. 1998, in IAU Colloq. 166, The Local Bubble and Beyond, ed. D. Breitschwerdt, M. J. Freyberg, & J. Truemper (Berlin: Springer), 103
Umetsu, K., Medezinski, E., Nonino, M., et al. 2014, ApJ, 795, 163
van Moorsel, G., Kemball, A., & Greisen, E. 1996, in ASP Conf. Ser. 101, Astronomical Data Analysis Software and Systems V, ed. G. H. Jacoby & J. Barnes (San Francisco, CA: ASP), 37
van Weeren, R. J., Bonafede, A., Ebeling, H., et al. 2012a, MNRAS, 425, L36
van Weeren, R. J., Röttgering, H. J. A., Intema, H. T., et al. 2012b, A&A, 546, A124
Wachter, K., Leach, R., & Kellogg, E. 1979, ApJ, 230, 274
Wright, E. L. 2006, PASP, 118, 1711
Zhuravleva, I., Churazov, E., Arevalo, P., et al. 2015, MNRAS, 450, 4184
Zitrin, A., Fabris, A., Merten, J., et al. 2015, ApJ, 801, 44
Zitrin, A., Meneghetti, M., Umetsu, K., et al. 2013, ApJL, 762, L30
Zuhone, J. 2009, PhD thesis, University of Chicago
ZuHone, J. A., Markevitch, M., & Johnson, R. E. 2010, ApJ, 717, 908